

ABSTRACT

Title of Thesis: EXPERIMENTAL INVESTIGATION OF LIQUID AND
GAS FUELED FLAMES TOWARDS THE
DEVELOPMENT OF A BURNING RATE EMULATOR
(BRE) FOR MICROGRAVITY APPLICATIONS

Michael J. Bustamante, Master of Science, 2012

Dissertation directed by: Associate Professor Peter B. Sunderland
Department of Fire Protection Engineering

Professor Emeritus James G. Quintiere
Department of Fire Protection Engineering

Laminar steady burning on flat plates was studied at various orientations with respect to gravity. Flat wicks were saturated with methanol or ethanol. Steady flames were obtained, and ranged from boundary layer flames to plume-type burning. Maximum burning rate per unit area was recorded at an upward inclination of 30°. Mass flux decreased with increasing wick length for all orientations. Dimensionless correlations, using a Rayleigh number and the orientation angle, collapsed most of the data, but not for the horizontal and vertical cases. The measured heat flux correlated with expected averages based on burning rate data; theoretical results were similar but radiation likely affected the wicks results. Gas burner flame stand-off distances when emulating methanol flames were in reasonable agreement, showing similarities in laminar, onset of turbulent flow, and boundary layer separation. 0g ethanol wick flames from drop tower testing and airplane testing are shown.

EXPERIMENTAL INVESTIGATION OF LIQUID AND GAS FUELED FLAMES
TOWARDS THE DEVELOPMENT OF A BURNING RATE EMULATOR (BRE) FOR
MICROGRAVITY APPLICATIONS

By

Michael J. Bustamante

Thesis submitted to the Faculty of the Graduate School of the
University of Maryland, College Park in partial fulfillment
of the requirements for the degree of
Master of Science
2012.

Advisory Committee:

Associate Professor Peter B. Sunderland, Chair

Professor Marino di Marzo

Professor Emeritus James G. Quintiere

Assistant Professor Stanislav I. Stoliarov

© Copyright by
Michael Joseph Bustamante
2012

Acknowledgements

This work was supported by a NASA Office of the Chief Technologist's Space Technology Research Fellowship (NASA Grant NNX11AN68H with grant monitor D. Urban). This work was also funded by NASA Grant NNX10AD98G, with P. Ferkul as technical contact.

There are several people and organizations I owe a debt of gratitude to in reference to my education and progress on this thesis. As mentioned above, NASA funds this project through a combination of grants, one of which is in the form of my fellowship. Without this funding this work would not have been possible, and this tremendous opportunity never would have presented itself. Thank you to everyone at NASA. In particular though I would like to thank Dr. Paul Ferkul and Dr. David Urban, my two points of contact there for these grants. Their expertise and support with this project has been invaluable.

I have been fortunate enough in my time at Maryland to overlap with a program that brings over German interns for several months at a time. Each of these individuals have contributed to this project in several ways and for that I am very thankful. To Michael Huis, Michael Lutz, Martin Willnauer, and Eric Meuller, it was nice being able to work with each of you and I thank you for all your help.

I could not have been as happy and enjoyed my graduate education anywhere else as much as I did here at the University of Maryland. This department is composed of an amazing set of people, without exception, and made my brief stay in this area a very memorable and pleasant one. Over the course of the past two years I have formed many new friendships I can only hope will endure for a lifetime. Thank you all for your

kindness, your help, and your smiles. Most of all though I need to recognize my advisers, Dr. Peter Sunderland and Dr. James Quintiere. I will be hard pressed to ever find myself in a situation where I get to work with people so knowledgeable, passionate, and friendly. Thank you both for your patience, your counsel, and your friendship. I was intimidated coming into graduate school, and unsure how I would like the arrangement; however now that I am almost done I am very sorry to go and I primarily owe this to the both of you.

Last but certainly not the least, I need to thank my parents, my siblings, and my new wife. I owe all of my academic success to my parents, for the habits and values ingrained in me from an early age have made me the person I am today. From care-packages to late night games and phone calls, you kept me sane through the busy and stressful times keeping me motivated and productive. Starting almost six years ago now I have been fortunate enough for Angela to be a large part of my life and just about two months before this will be submitted we were married. Ever since our beginning I have been happier than any one person deserves, I cannot thank you enough for your continued support and the overwhelming bliss you have introduced into my life.

Table of Contents

List of Figures.....	vi
List of Tables.....	x
List of Symbols.....	xi
1. Introduction	
1.1. Motivation and Objectives.....	1
1.2. Literature summary	
1.2.1. Burning with Liquid Soaked Wicks.....	2
1.2.2. Using Gas Burners in Condensed Phase Burning Research.....	4
1.2.3. Simulating Methanol Flames at Varying Orientations.....	4
1.3. Gas Burner Rationale.....	5
1.4. Mathematical Model.....	7
2. 1g Testing	
2.1. Experimental Set-up and Procedure	
2.1.1. Liquid Fuel Tests	
2.1.1.1. Test Apparatus and Wick Development.....	16
2.1.1.2. Final Test Apparatus and Wick Design.....	23
2.1.1.3. Testing Set-up.....	25
2.1.1.4. Test Procedure.....	25
2.1.1.5. Test Matrix.....	27
2.1.2. Gas Burner Tests	
2.1.2.1. 1 st Prototype Design.....	30
2.1.2.2. 1 st Prototype Testing Set-up.....	31
2.1.2.3. 1 st Prototype Test Procedure.....	31
2.1.2.4. 2 nd Prototype Design.....	32

2.1.2.5.	Gas Fuel Test Matrix.....	33
2.2.	Experimental Results and Discussion	
2.2.1.	Flame Stand-off Distance Measurements.....	34
2.2.2.	Burning Rate Measurements.....	38
2.2.3.	Heat Flux Measurements.....	43
3.	0g Testing	
3.1.	Experimental Set-up and Procedure	
3.1.1.	0g Airplane Tests	
3.1.1.1.	Simulating Microgravity with an Airplane.....	44
3.1.1.2.	Test Apparatus and Wick Design.....	45
3.1.1.3.	Test Procedure.....	47
3.1.1.4.	Aircraft Test Matrix.....	49
3.1.2.	0g Drop Tower Tests	
3.1.2.1.	Simulating Microgravity with a Drop Tower.....	50
3.1.2.2.	Test Apparatus and Wick Design.....	51
3.1.2.3.	Test Procedure.....	53
3.1.2.4.	Drop Tower Test Matrix.....	55
3.2.	Experimental Results and Discussion	
3.2.1.	Flame Shape Photographs.....	56
4.	Conclusions.....	61
Appendix		
	Appendix A: 1g Methanol Experimental Data.....	63
	Appendix B: 1g Ethanol Experimental Data.....	80
	Appendix C: 0g Ethanol Experimental Observations.....	82
	Appendix D: Observed Transition to Unsteadiness.....	88
	References.....	89

Table of Figures

Figure 1: Sketch of the theoretical model.....	8
Figure 2: Schematic of test stand utilized for liquid wick testing.....	16
Figure 3 Final wick design schematic. Width is held constant at 10 cm while wicks of length (ℓ) 1, 2, 3, 4, 6, 8, and 10 cm were constructed.....	17
Figure 4: Measured mass and rear temperature of ethanol soaked wicks to test thickness effect.....	19
Figure 5: Measured heat flux at center of 10 x 10 cm wick for multiple tests burning methanol at angles +90° (pool) and +60° with 15-20 °C water.....	20
Figure 6: Measured heat flux at center of 10 x 10 cm wick for multiple tests burning methanol at angles +90° (pool) and +60° with 65-70 °C water.....	21
Figure 7: Mass measurements examining the effect of the presence of the wick on the burning rate of the fuel. Three tests are shown for both the pool fire and wick test set-ups.....	22
Figure 8: Front and side views of liquid wick stand, with clamped in wick.....	23
Figure 9: Liquid fuel wick measuring 10 x 10 cm. Center hole accommodation allows for the heat flux gauge to pass through and be positioned level with the surface.....	24
Figure 10: Testing set-up for 1g burning rate, liquid fuel wicks. Nikon D70 is used to take the still images.....	27
Figure 11: First gas burner prototype schematic.....	30
Figure 12: Schematic of second gas burner prototype.....	32
Figure 13: Enhanced color images of flames fueled by methanol on 10 x 10 cm wicks (top) and methane through a 10 x 10 cm burner (bottom).....	34
Figure 14: Snap shots of flames fueled by methanol for all sizes and orientations.....	35
Figure 15: Measured flame heights examples from various tests at all orientations. Approximate areas where steady laminar (S.L.) and unsteady (U) behavior was observed are labeled. Methane flames simulated methanol wicks. Methanol model results with and without the cross-flow (CF) effects, and Ali et al.'s [4] DNS results are included.....	37
Figure 16: Average mass flux of methanol and ethanol as a function of angle for wick lengths of 1, 4, and 10 cm at angles ranging from -90° to +90°. Experimental (top) and model (bottom) results are included.....	38

Figure 17: Average mass flux from model and experimental results of methanol and ethanol for wick lengths of 1, 2, 3, 4, 6, 8, and 10 cm at angles from -90° to $+90^\circ$. Model results including the CF effect ($dp/dy \neq 0$) and excluding the CF effect ($dp/dy = 0$) have been included.....	41
Figure 18: Burning rates of methanol and ethanol plotted with respect to the modified Rayleigh number with the orientation angle correction. The line is the theory of Ahmad and Faeth [3].....	42
Figure 19: Local heat flux and average burning rate measured at $x = 5$ cm for Methanol soaked wicks, and at angles ranging from -90° to $+90^\circ$. Numerical results for the integral analysis are also included.....	43
Figure 20: Flight path of airplane for 0g testing, from [18].....	44
Figure 21: Aircraft rig with testing chamber seen on right. Window provides view down the top of the wick.....	46
Figure 22: Drop tower model showing cut-away of structure.....	50
Figure 23: Drop tower vehicle being loaded into the top of the steel vacuum chamber. After positioning the vehicle a steel cap is then lifted into place (not pictured).....	51
Figure 24: Layout of drop tower stand showing wick location (circular wick shown but rectangular wick's pyrolysis area would be centered in the same spot), cover plate location, and wire igniter location. Dotted lines show the movement of the cover plate and wire igniter.....	52
Figure 25: Elliptical ethanol flame at 0-g. Burning area measures 1 cm x 4 cm, viewing 4 cm side.....	56
Figure 26: Ethanol elliptical flame in 0-g demonstrating observed spiraling behavior around its base.....	57
Figure 27: Image from first drop tower testing of an elliptical ethanol flame at 0-g. Burning area measures 1 cm x 4 cm, viewing 4 cm side.....	58
Figure 28: Image progression from drop tower testing of an elliptical heptane flame at 0g. Far left image is from shortly after dropping, and progresses to the right approximately every 1.2s till just before impact. Burning area measures 1 cm x 4 cm, viewing 4 cm side. Atmosphere: 30% O ₂ , 29.4 psi.	59
Figure 29: Several images of a spherical n-decane flame subjected to different levels of g-jitter from Struk et al. [19]. Orange line represents gravity direction and magnitude, first picture ~ 20 milli-g, and the other two ~ 15 milli-g.....	60
Figure 30: Methanol measured flame stand-off at $+60^\circ$	64

Figure 31: Data for methanol measured flame stand-off at +30°.....	66
Figure 32: Data for methanol measured flame stand-off at 0°.....	68
Figure 33: Data for methanol measured flame stand-off at -30°.....	70
Figure 34: Data for methanol measured flame stand-off at -60°.....	72
Figure 35: Data for methanol measured flame stand-off at -90°.....	74
Figure 36: Individual and average heat flux test readings for methanol on 10 x 10 wick at +90°.....	76
Figure 37: Individual and average heat flux test readings for methanol on 10 x 10 wick at +60°.....	76
Figure 38: Individual and average heat flux test readings for methanol on 10 x 10 wick at +30°.....	77
Figure 39: Individual and average heat flux test readings for methanol on 10 x 10 wick at 0°.....	77
Figure 40: Individual and average heat flux test readings for methanol on 10 x 10 wick at -30°.....	78
Figure 41: Individual and average heat flux test readings for methanol on 10 x 10 wick at -60°.....	78
Figure 42: Individual and average heat flux test readings for methanol on 10 x 10 wick at -90°.....	79
Figure 43: Snapshots from “Zero 2” Video.....	82
Figure 44: Snapshots from “Zero 3” Video.....	82
Figure 45: Snapshots from “Zero 4” Video.....	82
Figure 46: Snapshots from “Zero 5” Video.....	83
Figure 47: Snapshots from “Zero 6” Video.....	83
Figure 48: Snapshots from “Zero 8” Video.....	83
Figure 49: Snapshots from “Zero 11” Video.....	84
Figure 50: Snapshots from “Zero 12” Video.....	84
Figure 51: Snapshots from “Zero 13” Video.....	84
Figure 52: Snapshots from “Zero 14” Video.....	85

Figure 53: Snapshots from first drop, using Ethanol on a 1 x 4 cm wick. Ignition took place approximately 3 seconds before release. Flame showed unsteady behavior but lasted the duration of the drop.86

Figure 54: Snapshots from second drop, using Ethanol on a 1 x 4 cm wick. Ignition approximately a half second after release of the vehicle. Flame self-extinguished after about a second, the above photographs are not every second, instead they were chosen more frequently to show in which way the flame extinguished.....86

Figure 55: Snapshots from third drop utilizing Ethanol on a circular pyrolysis area with equivalent area to the 1 x 4 cm rectangular wicks used in the previous two drops. Ignition approximately a half second before release. Although difficult to see, flame was sustained for duration of the drop.....86

Figure 56: Snapshots from fourth drop utilizing Ethanol on a 5 cm diameter circular wick. Ignition took place approximately a half second before release. Flame Self extinguished between 1 and 2 seconds after release.....87

Figure 57: Snapshots from fifth drop utilizing Ethanol on a 5 cm diameter circular wick in 30% oxygen atmosphere. Ignition approximately a half second before release. Flame sustained for entire duration of the drop. Flame front expanded slowly over the course of the drop.....87

Figure 58: Transition to unsteadiness as a function of orientation. Range shows maximum and minimum observed in the five analyzed flame stand-off photographs.....88

List of Tables

Table 1: Fuel properties from References [1,2].....	15
Table 2: Mass loss rate and accompanying linear fit R^2 values associated with the “wick effect” tests.....	22
Table 3: 1g Liquid Fuel Test Matrix.....	29
Table 4: 1g Gas Fuel Test Matrix.....	33
Table 5: 0g Liquid Fuel Airplane Test Matrix.....	49
Table 6: 0g Liquid Fuel Drop Tower Test Matrix.....	55
Table 7: Ethanol Flames at 14.5 – 15.0 psi and 0-g.....	57
Table 8: Drop Tower Testing Summary.....	60
Table 9: 1g Methanol Experimental Data.....	63
Table 10: Data for methanol measured flame stand-off at $+60^\circ$	64
Table 11: Data for methanol measured flame stand-off at $+30^\circ$	66
Table 12: Data for methanol measured flame stand-off at 0°	68
Table 13: Data for methanol measured flame stand-off at -30°	70
Table 14: Data for methanol measured flame stand-off at -60°	72
Table 15: Data for methanol measured flame stand-off at -90°	74
Table 16: 1g Ethanol Experimental Data.....	80

List of Symbols

		\dot{q}''	heat flux
a	eq. 35	\dot{q}_{rrr}''	re-radiation heat flux, eq. 1
b	eq. 36	Ra_l^*	Modified Rayleigh number, eq. 45
B	Spalding B number	s	oxygen to fuel stoichiometric ratio
c	eq. 39	S	$\frac{Y_{O_2,\infty}}{sY_{F,T}}$
c_p	specific heat of gas	Sc	Schmidt number
\bar{c}_p	mean specific heat	T	temperature
D	species diffusion coefficient	u	velocity along plate direction
g	gravity force per unit mass	U	$\frac{u_0 \delta}{\nu_\infty}$
Gr_x	Grashof number	v	velocity normal to plate
	modified Gr_x ,	w	$\rho v + u \int_0^y \left(\frac{\partial \rho}{\partial x}\right)_y dy$
Gr_x^*	$\frac{g \cos \theta L}{4\bar{c}_p T_\infty} \frac{l^3}{\nu_\infty^2}$	x	coordinate along plate
h	heat transfer coefficient	y	coordinate normal to plate
ΔH_c	heat of combustion	y_f	flame standoff distance
k	thermal conductivity	Y	direction with gravity vector
l	plate length	Y	Mass fraction
L	latent heat of vaporization	z	$z = \int_0^y \frac{\rho}{\rho_\infty} dy$
\dot{m}''	mass flow per unit area	β	Shab-Zel'dovich variable
\dot{m}'''	mass flow into unit volume	δ	boundary layer thickness
p	Pressure		
\tilde{p}	dynamic pressure		
p_s	static pressure		
Pr	Prandtl number		

Δ	$\frac{\delta}{l}$
ζ	$\frac{z}{\delta}$
θ	angle between x and Y
μ	dynamic viscosity
ν	kinematic viscosity
ξ	$\frac{x}{l}$
ρ	density
$\bar{\rho}$	mean density
Φ	enthalpy per unit mass
σ	Stefan-Boltzmann constant
τ_0	$\frac{\bar{c}_p(T_w - T_\infty)}{L}$

Subscripts

O	initial
<i>f</i>	flame
<i>F</i>	Fuel
<i>T</i>	condensed phase
<i>i</i>	species
<i>ox</i>	oxygen
<i>w</i>	wall (gas phase)
s	surface
∞	ambient

1. Introduction

1.1. Motivation and Objective

A necessity for safe space flight and exploration is an understanding of how or if materials will burn in space. Ideally, the work done under the supporting grants will ultimately result in a single compact device that could simulate a wide range of solids and liquids with only minimal changes between tests. Specifically, the grants' proposed BRE apparatus would emulate these materials through control of the gas flow rate via feedback from an embedded heat flux meter, control of the surface temperature using a heat exchanger, dilution of fuel with inert gases, and possibly the use of a few different gaseous fuels with a range of properties. The resulting apparatus could then scan through a practical spectrum of real fuels to identify what properties are essential for quiescent burning in microgravity conditions.

In order to properly test the burner under gravity conditions and prove the end design, a dataset for comparison purposes is necessary. It was decided that the benchmark would be burning on flat plates at varying angles of orientation. Methanol and Ethanol saturated wicks were chosen for this initial testing to facilitate easy steady burning. Pool fires were compared to the wick fires to show that they burn nearly the same. A mathematical model was also developed to look at the potential for theory to accurately predict the burning. The data and conclusions resulting from these experiments are presented in this thesis.

During the course of this work opportunities arose to begin testing in microgravity. Liquid wicks were burned in both an airplane and a drop tower in 0g.

These burns were used to examine the propensity of these fuels to burn steadily in a quiescent environment.

Following these liquid tests, work under these grants have been started towards development of the BRE using gas burners. Results for a rectangular gas burner has been compared within. The next iteration of the BRE incorporates several improvements in controls and a redesign which no longer retains a shape similar to the liquid wicks we tested with. This shift in size and shape stems from a change in directive as the original goal was for testing exclusively on the airplane. Since the scope of the project has changed to hopefully lead to testing on the space station this would now be exclusively 0-g testing. Results from this burner will be included in future publications and work currently being pursued by Yi Zhang, Dr. Sunderland, and Dr. Quintiere.

To summarize, a challenging dataset utilizing square wicks and liquid fuels burning in gravity was first collected. A means of measuring heat flux to the surface was then implemented. Next, a first stage gas burner prototype was constructed and used to emulate the liquid flames while in tandem a mathematical model was developed. Airplane and drop tower 0g testing was conducted to investigate the prospect of steady quiescent burning, and lastly, the design and construction of the second prototype gas burner with a round configuration was completed.

1.2. Literature Summary

1.2.1. Burning with Liquid Soaked Wicks

The use of fuel-soaked wicks was first pioneered by Blackshear and Murty [6], who focused on the study of the free-convection heat-and-mass transfer coefficients and

found that orientation, size, and shape all have a minimal effect on coefficients for turbulent flames. Continued work [5] examining the effects of size, orientation, and fuel molecular weight on vertical and horizontal fuel-soaked wicks concluded that burning rates of wicks agree with those of flowing vertical films and stationary horizontal pools, as well as, for sizes 1 - 20 cm the burning rate is primarily controlled by convection. Kim et al. [11] presented a generalized solution for the free-convective laminar burning of vertical, inclined, and horizontal cylinders that compared well with experimental results from experiments involving low molar mass fuels. In particular the results showed that the chemical effects are a function of the Spalding mass transfer number, B , while the geometric effects are a function of the Grashof number, Gr . Related work by Kosdon et al. [12] investigated burning of vertically oriented cylinders and developed a similarity theory for the natural-convection boundary layer adjacent to a vertical plate.

Ahmad and Faeth [1,2,3,10] utilized methanol, ethanol, and propanol soaked wicks to investigate the laminar burning and the overfire region during natural convective burning on an upright surface and presented a similarity solution and integral models for both laminar and turbulent burning. Their results for predicted flame shapes and heat fluxes were found to be within 20% of measurements.

Work studying the effect of the presence of a wick on the burning rate of liquid fuels [20] revealed several factors. Neighboring fuel tended to cover surface discontinuities, but burning rates for partially covered surfaces were still found to be less. Porosity and permeability are suggested for wick design to achieve sufficient capillary pressure without overwhelming resistance to liquid flow but minor deviations from ideal liquid film covered surface burning behavior is expected.

1.2.2. Using Gas Burners in Condensed Phase Burning Research

Sintered metal gas burners have been used to emulate the burning of liquids and solids in the vertical [8] and ceiling [14,15] orientations by utilizing fuel-inert mixtures. Results showed that the burning rate was controlled by the B number, and that by varying composition and flow rates a controlled simulation of a wide range of solids and liquids could be achieved.

1.2.3 Simulating Methanol Flames at Varying Orientations

Recently a numerical study by Ali et al. [4] studied the effect of the fuel surface being at an angular orientation using methanol as a fuel. Maximum burning rates were observed between -45° and -30° (upward facing measured from vertical). These were direct numerical solutions to the full conservation equations and consequently were limited to a small burning domain of 1 cm.

1.3. Gas Burner Rationale [7]

While gas burners have been used to successfully emulate burning rate [8,14,15], we wanted to offer a rationale for their use. A more complete analysis might compare solutions for burning to the uniform distribution of a gas burner, but that would be tedious. Instead we consider a physical model.

For steady evaporative burning, with a blackbody surface is

$$\dot{m}''L = \dot{q}_f'' - \underbrace{\sigma(T_s^4 - T_\infty^4)}_{\dot{q}_{rr}''} \quad (1)$$

The re-radiation is small as long as $T_s < 200$ °C, e.g.. for $T_s = 200$ °C, $\dot{q}_{rr}'' = 2.4$ kW/m² when the flame heat flux is expected to generally be greater than 20 kW/m². From burning rate theory under pure convection flame heating

$$\dot{m}'' \approx \frac{k}{c_p \delta} B \quad (2)$$

where δ is the boundary layer thickness with blowing, and the Spalding B-number is:

$$B \equiv \frac{Y_{O_2,\infty} \Delta H_c / s - c_p (T_s - T_\infty)}{L} \quad (3)$$

For small $T_s - T_\infty$:

$$B \approx \frac{Y_{O_2,\infty} \Delta H_c / s}{L} \quad (4)$$

The burner gives L , based on measuring \dot{q}_f'' for a given fuel flow rate. Then from Eq. (4) B is given for the same fuel. We infer from Eq. (2) that the burner with the same \bar{m}'' and B of the burning fuel also has a same boundary layer thickness (δ).

For no blowing in pure natural convection the boundary layer thickness without burning (δ_o) is related to δ by the blowing factor:

$$\delta = \delta_o \frac{B}{\ln(1+B)}, \quad \delta > \delta_o \quad (5)$$

and for laminar natural convection

$$\delta_o / x \sim Gr_x^{-1/4} \quad \text{where} \quad Gr_x = g \cos \theta x^3 / \nu_\infty^2 \quad (6)$$

As such, δ_o depends on orientation and configuration in general. Therefore, for the same configuration, and with a simulated B of the fuel, δ represents the burning behavior of the simulated fuel.

Finally, the flame position y_f can be represented in terms of the boundary layer from stagnant layer burning theory [16] as

$$\frac{y_f}{\delta} = 1 - \frac{\ln(1 + Y_{ox,\infty} / s)}{\ln(1 + B)}. \quad (7)$$

This indicates that y_f should be the same for the burner as it is for fuel with same value L .

All the prior justifications for the burner are based on the assumption that the average mass loss flux of the burner distributes itself to burn in a similar fashion to that represented by L . In short, selecting a value for L to emulate gives the associated B value response. Measuring \dot{q}_f'' , when T_s is low enough, gives $\dot{m}'' = \dot{q}_f'' / L$, and accordingly y_f and δ should be the same.

We will test the burner concept by using the wick experiments in which L and $\overline{\dot{m}}''$ are known from measurement with methanol soaked wicks. For the same configuration the burning rate of methanol is matched with a flow rate of methane

through the burner. For a matching configuration, we examine if the flame stand-off position is simulated.

Here methane is used to simulate methanol. The fuels have different heats of combustion, and slightly different radiation properties. The heat of combustion combined with the generally invariant heat of combustion per unit mass of air leads to differing stoichiometric air to fuel (A/F) ratios. The stoichiometric A/F ratio will control the vertical flame height away from the surface and differences will be seen here, but not in the flame near the surface as presented by the boundary layer physics above.

1.4. Mathematical Model

The mathematical model that follows was an effort spearheaded by collaborators Dr. James Quintiere and Yi Zhang (personal communication 2011-2012 and [7]). All numerical solutions shown later in this thesis were provided by Yi Zhang.

This mathematical model was pursued to examine burning characteristics at various angles. Theoretical models developed in the literature ignore the normal pressure gradient, on the premise that it is a relatively small effect, and in doing so do not capture what side the burning is taking place on (for inclinations). As such the theory was extended to evaluate it against the data.

The model addresses laminar, two-dimensional steady natural convection burning on a flat plate at various orientations as shown in Figure 1. Negative angles correspond to burning underneath the plate. The model follows that of Ahmad and Faeth [1,2], except the normal pressure gradient is considered. This effect comes from the normal momentum equation, and produces an additional buoyancy term that aligns with the main

flow direction. It will be called “the cross-flow effect (CF)”. This effect is included to help differentiate between burning at the top and the bottom for the same inclination. The following are the conditions of the model:

- The ambient has a constant temperature and composition.
- Density does not change strongly with x .
- Flames are laminar, two dimensional and steady.
- Boundary layer assumption.
- The flow is a mixture of ideal

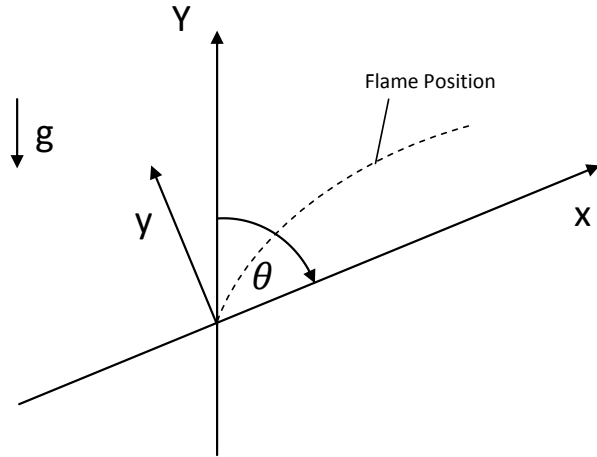


Figure 1. – Sketch of the theoretical model

- gas with constant specific heat, and unity Lewis number.
- Radiation and viscous dissipation are neglected.
- The combustion process is a single global chemical reaction.
- Flame sheet assumption.

The pressure is decomposed into perturbation and static terms.

$$p = \tilde{p} + p_s \quad (8)$$

$$\frac{dp_s}{dY} = -\rho_\infty g \quad (9)$$

$$Y = x \cos \theta + y \sin \theta \quad (10)$$

The boundary layer conservation equations are:

Mass:
$$\frac{\partial(\rho u)}{\partial x} + \frac{\partial(\rho v)}{\partial y} = 0 \quad (11)$$

Momentum:

$$\rho \left(u \frac{\partial u}{\partial x} + v \frac{\partial u}{\partial y} \right) = \frac{\partial}{\partial y} \left(\mu \frac{\partial u}{\partial y} \right) - \left(\frac{\partial \tilde{p}}{\partial y} \right) + (\rho_\infty - \rho) g \cos \theta \quad (12)$$

$$0 = - \left(\frac{\partial \tilde{p}}{\partial y} \right)_x + (\rho_\infty - \rho) g \cos \theta \quad (13)$$

Energy:

$$\rho \left(u \frac{\partial \Phi}{\partial x} + v \frac{\partial \Phi}{\partial y} \right) = \frac{\partial}{\partial y} \left(\frac{k}{c_p} \frac{\partial \Phi}{\partial y} \right) + \dot{m}_f''' \Delta H_c \quad (14)$$

$$\text{with } \Phi = \int_{T_\infty}^T c_p dT \cong \bar{c}_p (T - T_\infty) \quad (15)$$

Species:

$$\rho \left(u \frac{\partial Y_i}{\partial x} + v \frac{\partial Y_i}{\partial y} \right) = \frac{\partial}{\partial y} \left(\rho D \frac{\partial Y_i}{\partial y} \right) + \dot{m}_i''' \quad (16)$$

The one-step reaction is presented as the mass-based stoichiometric equation



Pressure is constant, so the ideal gas theory gives $\rho T = \rho_\infty T_\infty$ or

$$\frac{\rho_\infty - \rho}{\rho} = \frac{T - T_\infty}{T_\infty} = \frac{\Phi}{c_p T_\infty} \quad (17)$$

Equations are transformed into incompressible form by introducing $z = \int_0^y \frac{\rho}{\rho_\infty} dy$, in

which $z = z(x, y)$. Also $\rho \mu$ is assumed to be constant. Shab-Zel'dovich (S-Z) variables

are introduced as follows:

$$\beta_{\Phi O} = \Phi + \frac{Y_O \Delta H_c}{s} \quad (18)$$

$$\beta_{\Phi f} = \Phi + Y_f \Delta h_c \quad (19)$$

$$\beta_{FO} = Y_F + \frac{Y_O}{s} \quad (20)$$

Furthermore,

$$\text{Pr} = \frac{\mu c_p}{k} = 1 \quad \text{and} \quad \text{Sc} = \frac{\mu}{\rho D} = 1$$

A dimensionless mixture fraction is introduced:

$$\beta^* = \frac{\beta_i - \beta_{i,\infty}}{\beta_{i,w} - \beta_{i,\infty}} \quad (21)$$

in which “w” implies wall conditions: $y = 0$ $z = 0$ and ∞ implies ambient conditions:

$y \rightarrow \infty$ $z \rightarrow \infty$. The equations then become:

$$L[u] = \left(\frac{\rho_\infty - \rho}{\rho} \right) g \cos \theta - \frac{1}{\rho} \left(\frac{\partial \tilde{p}}{\partial x} \right)_y \quad (22)$$

where:

$$L[] \equiv u \frac{\partial}{\partial x} + w \frac{\partial}{\partial z} - \frac{\partial}{\partial z} (\rho \mu) \frac{\partial}{\partial z}, \quad w = \rho v + u \int_0^y \left(\frac{\partial \rho}{\partial x} \right)_y dy$$

The pressure gradient term in Eq. (22) can be found by the chain rule as

$$\begin{aligned} \left(\frac{\partial \tilde{p}}{\partial x} \right)_y &= \left(\frac{\partial \tilde{p}}{\partial x} \right)_z + \left(\frac{\partial \tilde{p}}{\partial z} \right)_x \left(\frac{\partial z}{\partial x} \right)_y \\ &= - \frac{\partial}{\partial x} \int_z^\infty \left(\frac{\rho - \rho_\infty}{\rho} \right) g \sin \theta dz + \left(\frac{\rho - \rho_\infty}{\rho} \right) g \sin \theta \int_0^y \left(\frac{\partial \rho}{\partial x} \right)_y dy \end{aligned}$$

Invoking slow variation of density in the x direction allows $\left(\frac{\partial \rho}{\partial x} \right)_y \approx 0$, $\rho \rightarrow \bar{\rho}$, a mean

density. Then the operator becomes over the velocity and mixture fraction as

$$L[u] = \left(\frac{\rho_\infty - \rho}{\rho} \right) g \cos \theta + \frac{g \sin \theta}{\bar{\rho}} \frac{\partial}{\partial x} \int_z^\infty \left(\frac{\rho_\infty - \rho}{\rho} \right) dz \quad (23)$$

$$L[\beta^*] = 0$$

The second term on the left hand side of the momentum equation is the “cross-flow effect”. The boundary conditions follow as:

$$x = 0: u = 0, \beta^* = 0$$

$$z = 0: u = 0, \quad \beta^* = 1, w = -\frac{\rho\mu}{\rho_\infty Pr} B \left(\frac{\partial \beta^*}{\partial z} \right)_{z=0},$$

$$\text{where } B = \frac{Y_{o,\infty} \Delta h_c - \Phi_w}{S L}$$

$$z \rightarrow \infty: u = 0, \frac{\partial u}{\partial z} = 0, \quad \beta^* = 0, \frac{\partial \beta^*}{\partial z} = 0$$

From the relationship between density, temperature and enthalpy along with the S-Z variable definitions it can be shown that [1,3]

$$\frac{\rho_\infty - \rho}{\rho} = \frac{L}{\bar{c}_p T_\infty} \left[\left(B + \frac{\Phi_w}{L} \right) - B\beta^* \right] \quad 0 \leq \zeta \leq \zeta_f \quad (24)$$

$$\frac{\rho_\infty - \rho}{\rho} = \frac{L}{\bar{c}_p T_\infty} \left(\frac{B + \frac{\Phi_w}{L}}{\beta_f^*} - B \right) \beta^* \quad \zeta_f \leq \zeta \leq 1 \quad (25)$$

$$\beta_f^* = \left(\frac{B+1}{B} \right) \left(\frac{S}{S+1} \right), \zeta_f = 1 - \beta_f^{*1/3}, \quad S \equiv \frac{Y_{o,\infty}}{S Y_{F,T}}, Y_{F,T} \equiv 1 \quad (26)$$

To facilitate an integral solution, the equations are integrated across the boundary layer to form ordinary differential equations:

$$\begin{aligned} \frac{d}{dx} \int_0^\infty u^2 dz + \left(\frac{\mu_\infty}{\rho_\infty} \right) \left(\frac{\partial u}{\partial z} \right)_{z=0} \\ = \int_0^\infty \left(\frac{\rho_\infty - \rho}{\rho} \right) g \cos \theta dz + \frac{g \sin \theta}{\bar{\rho}/\rho_\infty} \frac{d}{dx} \int_0^\infty z \left(\frac{\rho_\infty - \rho}{\rho} \right) dz \end{aligned} \quad (27)$$

$$\frac{d}{dx} \int_0^\infty (u\beta^*) dz + \frac{\nu_\infty}{Pr} (B+1) \left(\frac{\partial \beta^*}{\partial z} \right)_{z=0} = 0 \quad (28)$$

In which $\frac{\rho\mu}{\rho_\infty^2} = \frac{\mu_\infty}{\rho_\infty} \equiv \nu_\infty$, the kinematic viscosity. A new z-variable is introduced and profile functions are introduced for u and β .

$$\int_0^{\infty} dz \rightarrow \delta \int_0^1 d\zeta, \zeta \equiv \frac{z}{\delta} \quad (29)$$

The profiles satisfy the natural boundary conditions above and derived conditions:

$$\frac{\partial^2 u}{\partial z^2} = \text{function}(x) \text{ at } z = 0$$

and

$$\frac{\partial^2 \beta}{\partial z^2} = 0 \text{ at } z \rightarrow \infty.$$

The resulting profiles follow from [1,3]

$$u = u_0(x)\zeta(1-\zeta)^2 \quad (30)$$

$$\beta^* = (1-\zeta)^3 \quad (31)$$

Because the derived boundary condition on velocity ignored mass transfer, a blowing correction term suggested by Marxman [13] with $\frac{\ln(1+B)}{B}$, included as a multiplying term

for the diffusive transport terms at the wall. The equations become:

$$\begin{aligned} & \left(\int_0^1 \zeta^2 (1-\zeta)^4 d\zeta \right) \frac{d(u_0^2 \delta)}{dx} + \mu_{\infty} \frac{\ln(1+B)}{B} \frac{u_0}{\delta} \\ & = g \cos \theta \delta \int_0^1 \left(\frac{\rho_{\infty} - \rho}{\rho} \right) d\zeta + \frac{g \sin \theta}{\bar{\rho} / \rho_{\infty}} \left[\int_0^1 \left(\frac{\rho_{\infty} - \rho}{\rho} \right) \zeta d\zeta \right] \frac{d(\delta^2)}{dx} \end{aligned} \quad (32)$$

$$\left(\int_0^1 \zeta (1-\zeta)^5 d\zeta \right) \frac{d(u_0 \delta)}{dx} + (-3) \frac{v_{\infty}}{Pr} \frac{(B+1) \ln(1+B)}{\delta B} = 0 \quad (33)$$

Let $\xi = \frac{x}{l}$, $U = \frac{u_0 \delta}{v_{\infty}}$, $\Delta = \frac{\delta}{l}$:

$$\frac{1}{105} \frac{d(U^2 \Delta)}{d\xi} + \frac{\ln(1+B)U}{B \Delta} = \left(\frac{g \cos \theta L}{4\bar{c}_p T_{\infty}} \frac{l^3}{v_{\infty}^2} \right) \left(a\Delta + \frac{b \tan \theta}{\bar{\rho} / \rho_{\infty}} \frac{d\Delta^2}{d\xi} \right) \quad (34)$$

$$\frac{1}{42} \frac{d(U\Delta)}{d\xi} - \frac{3(B+1)\ln(1+B)}{Pr} \frac{1}{B\Delta} = 0 \quad (35)$$

$$a \equiv 3(B + \tau_0)\zeta_f + \tau_0,$$

$$b \equiv \left(\frac{B + \tau_0}{S}\right)(6\zeta_f^2 + 3\zeta_f + 1) - \frac{B}{5}, \tau_0 = \frac{\Phi_w}{L} = \frac{\bar{c}_p(T_w - T_\infty)}{L} \quad (36)$$

Using initial conditions $\xi = 0, U = \Delta = 0$, solutions for U and Δ with regard to ξ can be found. The term containing b above is the cross-flow effect. When $b = 0$, analytically solutions can be found, otherwise a numerical solution must be rendered.

The burning rate and the flame stand-off distance can be formulated as follows:

Local burning flux:

$$\frac{\dot{m}_F'' l}{\mu_\infty} = \frac{3}{Pr} \frac{\ln(1+B)}{\Delta} \quad (37)$$

Average burning flux:

$$\frac{\bar{\dot{m}}_F'' l}{\mu_\infty} = \frac{3}{Pr} \ln(1+B) \int_0^1 \frac{d\xi}{\Delta} \quad (38)$$

Flame stand-off:

$$y_f = c\Delta l, \quad c \equiv \left(\frac{L}{4\bar{c}_p T_\infty}\right) \left[4(B + \tau_0)\zeta_f + B \left[(1 - \zeta_f)^4 - 1\right]\right] + \zeta_f \quad (39)$$

For $b = 0$, by which the cross-flow effect is neglected, the equations could be solved analytically as done previously by Ahmad and Faeth [1,2] giving:

$$U = \left[\frac{168a(1+B)Gr_l^*}{2(1+B) + Pr} \right]^{\frac{1}{2}} \xi^{\frac{1}{2}} \quad (40)$$

$$\Delta = \left[\frac{\ln(1+B)}{BPr} \right]^{\frac{1}{2}} \left[\frac{168(1+B)[2(1+B) + Pr]}{Gr_l^* * a} \right]^{\frac{1}{4}} \xi^{\frac{1}{4}} \quad (41)$$

In which $Gr_l^* = \frac{g \cos \theta L l^3}{4\bar{c}_p T_\infty \nu_\infty^2}$

Substituting U and Δ into the local burning rate and flame stand-off distance gives

$$\dot{m}_F'' = \frac{3\mu_\infty \ln(1+B)}{Pr} \left[\frac{BPr}{\ln(1+B)} \right]^{\frac{1}{2}} \left[\frac{\frac{g \cos \theta L}{4\bar{c}_p T_\infty \nu_\infty^2} * a}{168(1+B)[2(1+B) + Pr]} \right]^{\frac{1}{4}} x^{-\frac{1}{4}} \quad (42)$$

$$y_f = c \left[\frac{\ln(1+B)}{BPr} \right]^{1/2} \left[\frac{\frac{g \cos \theta L}{4\bar{c}_p T_\infty \nu_\infty^2} * a}{168(1+B)[2(1+B) + Pr]} \right]^{-1/4} x^{1/4} \quad (43)$$

The average mass burning flux is given by

$$\bar{m}'' l Pr^{2/3} \Sigma / \mu_\infty = 0.934 Pr^{-1/12} Ra_\ell^{*1/4} \quad (44)$$

Note: An error was found in Ahmad and Faeth's work which was corrected resulting in a coefficient of 0.934 instead of 0.66.

The modified Rayleigh number (Ra_ℓ^*) is:

$$Ra_\ell^* = Pr L g l^3 \cos(\theta) / (4c_p T_\infty \nu_\infty^2) \quad (45)$$

And the parameter Σ is defined as:

$$\Sigma = [(1+B)/(B \ln(1+B))]^{1/2} [1 + 0.5Pr/(1+B)] / [3(B + \tau_o)\zeta_f + \tau_o]^{1/4} \quad (46)$$

Both local burning rate and flame stand-off distance are independent of the overall plate length l .

For the b term not zero, the equations are solved numerically using Mathematica and values from Table 1. Due to singularity issues near the origin, the solution was

problematic and is only solved for limited cases. The results of the experiments will be compared to solutions with and without the cross-flow term.

Table 1. Fuel properties from Refs [1,2]

Property	Methanol	Ethanol
Molecular Weight (g/mol)	32.04	46.07
Boiling Temperature (K)	337.7	351.5
L (kJ/kg) ^b	1226	880
c _p (kJ/kg-K) ^b	1.37	1.43
μ _{air} (x 10 ⁻⁵) (N-s/m ²) ^b	1.8	2.08
B	2.6	3.41
r	0.154	0.111
τ ₀	0.044	0.087
Pr	0.73	0.73
ζ _f ^a	0.430	0.494
\bar{P}/ρ_∞ @ 1000 °C	0.234	0.234

Ambient air taken to be at 298K: $\nu_\infty = 15.3 \times 10^{-6} \text{ m}^2/\text{s}$.

^aCalculated parameter

^bTaken at boiling point of fuel

2. 1g Testing

2.1.1 Experimental Set-up and Procedure

2.1.1.1. Liquid Fuel Tests

2.1.1.1.1. Test Apparatus and Wick Development:

Testing of different size samples was desired at a full range of angles from ceiling (-90°) to pool (+90°) fire orientations. Accordingly the developed stand was required to rotate in such a fashion as to not obstruct a camera's line of sight, be capable of holding several different size wicks, and have a means of accommodating a heat flux sensor that will pass through to the surface of the attached wicks. The constructed stand accomplished these objectives by utilizing a hollow clamping assembly for attaching different size wicks, provided they have a proper mount, and simultaneously allowing for a heat flux sensor to be inserted in through to the top of the wick surface. The clamping assembly is attached to a levered arm so that a clear view of the wick surface is always available, as seen in Figure 2.

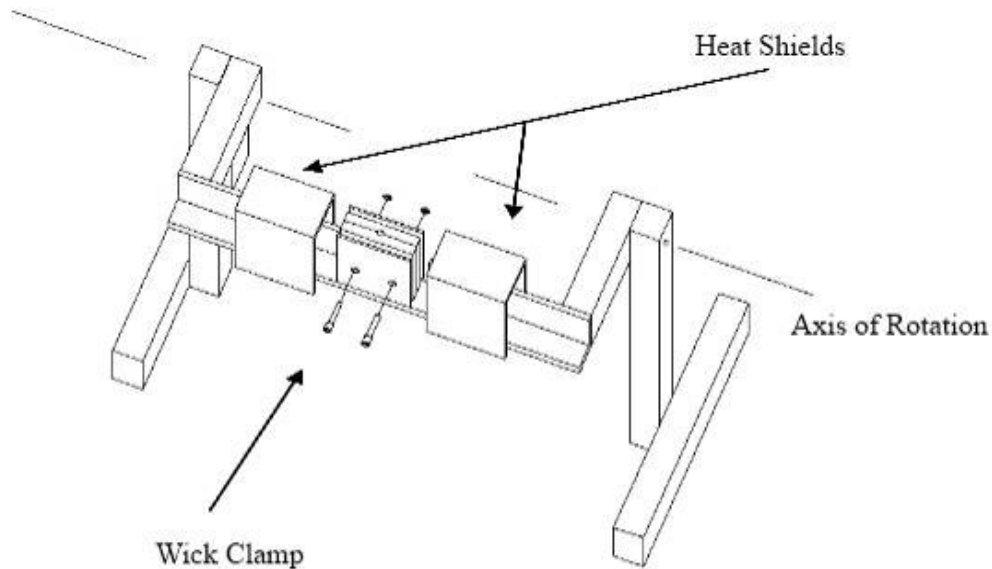


Figure 2. Schematic of test stand utilized for liquid wick testing.

Initial work on burning liquids with ceramic wicks for this project utilized 1.27 cm thick *Kaowool 3000* vacuum-formed insulation board wrapped with aluminum foil attached via high temperature silicone sealant. This wick performed well in the pool fire orientation but leaked beyond the vertical (0°) orientation. Testing with these wicks also showed that the high temperature silicone sealant had a tendency to burn when exposed to a flame, and that the amount of heat reentering the wick through the sides and rear of the wick was sufficient enough to increase the burning rate of the fuel.

A revised wick design, see Figure 3, utilizes 0.32 cm thick *Kaowool PM* board, a slightly denser material, and added a border. The new wick uses sodium silicate as a sealant to help prevent the fuel from entering the border and as an adhesive to attach the aluminum foil and border. The new design proved to be capable of inverted burning without any issue of dripping – a result of the density change, the thickness change, or some combination of both. This wick design was in place for the first set of tests of methanol and ethanol fuels on wick sizes of 1, 2, 3, 4, 6, 8, and 10 cm (x 10 cm) for 30°

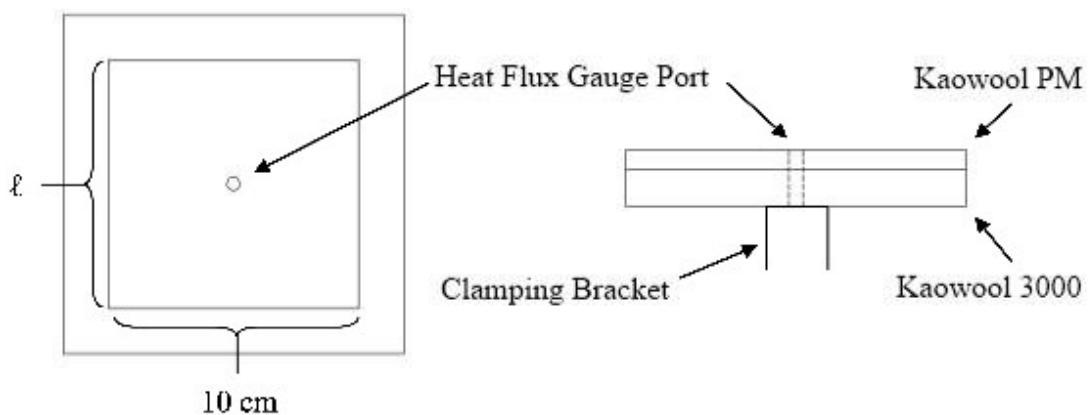


Figure 3. Final wick design schematic. Width is held constant at 10 cm while wicks of length (ℓ) 1, 2, 3, 4, 6, 8, and 10 cm were constructed.

increments between +90° and -90°.

Later changes included a larger border (increased from 2.5 to 5 cm) to prevent the flame from spilling over the edge of the wick during inverted testing, and a steel tube placed through the middle of the burning area to allow a heat flux gauge to be inserted to the top level of the wick. Comparing newer wick constructions to older constructions revealed that the Kaowool had expanded ~0.16 cm over the course of repeated testing, but a comparison of data showed this had no discernible effect on the burning rate.

A few issues of concern that arose during testing included: rear temperature of the wick and the accompanying heat loss, border thickness, condensation effects on the heat flux gauge, and effects from the presence of the wick material on the fuels burning rate.

To test the effect of the heat loss through the bottom, another wick with 0.95 cm thickness (triple the normal thickness) was constructed under the premise that not as much heat would be lost out the back due to the greater depth, which would include a larger portion of what would be the steady state isotherm condition. If a significant amount of heat was originally being lost out the back due to the fuel layer not being thick enough to absorb the penetrating heat, then a notable difference in burning rate would be observable. A set of tests, comparing the thick and thin wicks found a 1% difference in burning rates, a margin well within what would be expected in even repeated identical test setups for typical fire testing and accordingly this concern was dismissed – see Figure 4 for burning rate and rear temperature measurements.

An additional test run at this time was measurement of the surface temperature, which was confirmed to be approximately the boiling point of each respective fuel.

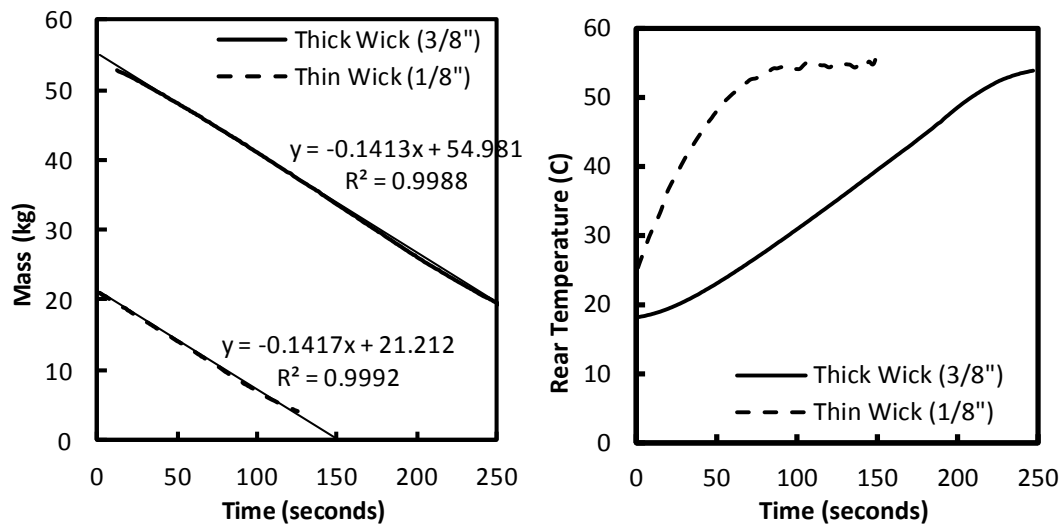


Figure 4. Measured mass and rear temperature of ethanol soaked wicks to test thickness effect.

Border thickness was raised as a concern after the 7th U.S. National Combustion meeting where a student studying flame spread on PMMA through the same range of angles noted a larger difference in burning rates when the pyrolysis region is surrounded with a thin border (comparing two centimeters to five centimeters in his case). To test if this effect is present in this work the border of the 2 x 10 cm wick was extended from 3 cm to 10 cm and additional burning rate tests were conducted. A 3% difference in burning rate was observed between the two testing set-ups, a difference that again fell within the amount of variation most likely due to the randomness of a fire, and hence it was concluded that the border was of sufficient width for all previously conducted testing.

When the heat flux gauge was initially incorporated into the wick, readings were inconsistent and displayed unexpected behavior. Seen in Figure 5, in the pool fire orientation the heat flux consistently was recorded having unexplained drops for a period

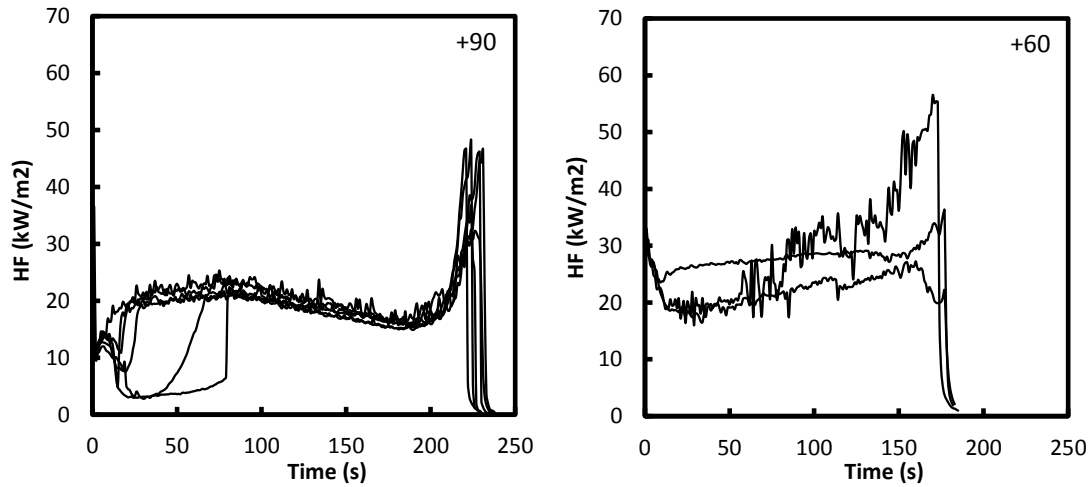


Figure 5. Measured heat flux at center of 10 x 10 cm wick for multiple tests burning methanol at angles +90° (pool) and +60° with 15-20 °C water.

of 10 – 60 s before returning to values that agree with other tests. while for the +60° orientation none of the three tests conducted at that angle had a general agreement with the other two. During these tests condensation was observed on the surface of the heat flux gauge in the form of a thin film or a larger droplet depending on the test. Repeating the tests with a water heater, which raised the temperature from ambient (20°C) to approximately 70°C, provided more stable and different magnitude heat fluxes as seen in Figure 6.

An additional advantage of the hot water is that it essentially eliminates the need to correct the readings for reradiation due to differences in surface temperature, an initially small impact to begin with. For example, in the case of methanol the surface temperature of the wick would near that of its boiling point, 64.7 °C (337.7 K), while the surface of the heat flux gauge would remain at the water temperature, 20 °C (293 K). Accordingly reradiation from the surface of the wick: $\dot{q}_{r,r}^m = \sigma(T_w^4 - T_{20}^4) \approx 0.320$ kW/m². In comparison, the heat flux gauge is operating with hot water its reradiation \approx

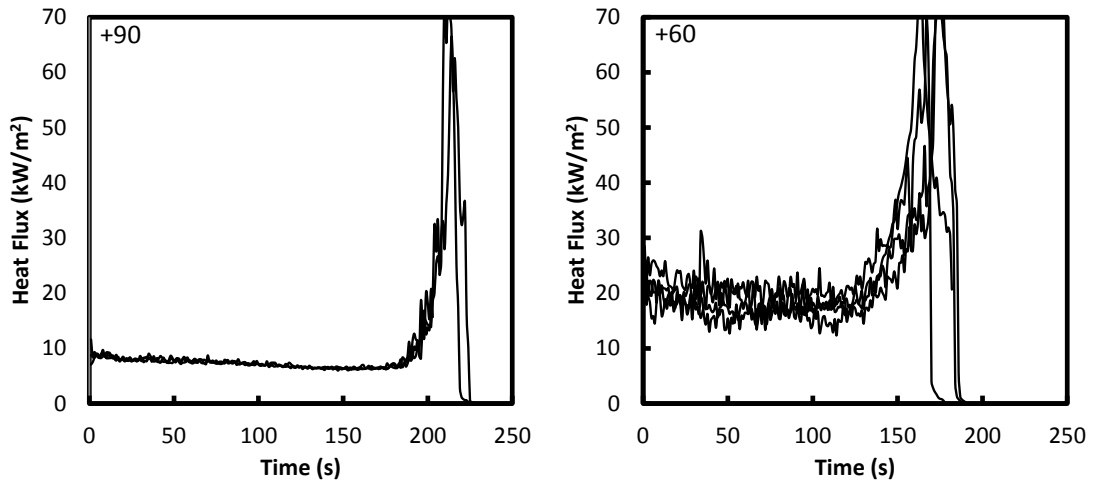


Figure 6. Measured heat flux at center of 10 x 10 cm wick for multiple tests burning methanol at angles +90° (pool) and +60° with 65-70 °C water.

0.367 kW/m², meaning a difference in reradiation of 0.047 kW/m², when typical measured heat fluxes are expected to be around 20 kW/m².

As mentioned previously [8], prior research has shown that the presence of the wick material can have a significant effect on the burning rate of the fuel. Ideally, a wick material would not be very dense – hence not significantly interrupting the fluid dynamics of the fuel being brought to the surface – and also the material would be inert so it does not participate in the combustion chemistry. However, as was seen with the *Kaowool 3000* board, if a chosen wick material is not dense enough it will fail to retain the fuel when used in an inverted position. As such it is critical to try to find a balance between the two qualities such that there is minimal impact on the process while still attaining the properties required to conduct testing all orientations. *Kaowool PM* met the density requirement and then was tested later for impact on burning rate. This was tested using a petri dish which was backed with *Kaowool 3000* and surrounded on the sides up to the lip with *Kaowool PM*. The petri dish was then filled completely with fuel and

burned for a short period before being extinguished. For wick testing the petri dish remained in place but was filled with *Kaowool PM* before adding the fuel and burning for a short period again. A 0.4% decrease was observed when a wick was introduced, see Figure 7 and Table 2, showing that the presence of *Kaowool PM* does not have a significant effect on the burning rate.

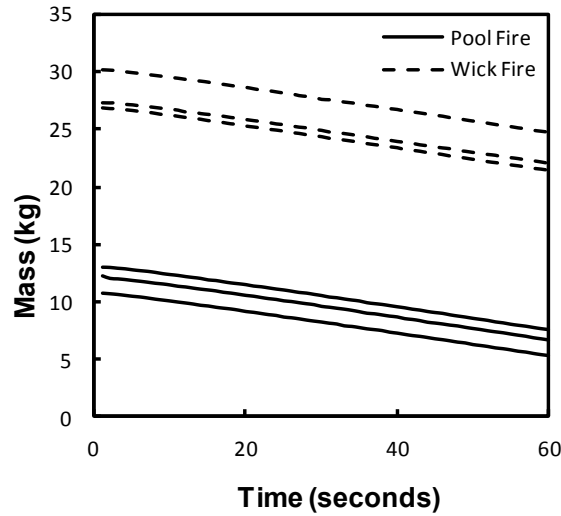


Figure 7. Mass measurements examining the effect of the presence of the wick on the burning rate of the fuel. Three tests are shown for both the pool fire and wick test set-ups.

Table 2. Mass loss rate and accompanying linear fit R^2 values associated with the “wick effect” tests.

Wick Fire	
Mass Loss Rate (kg/s)	R^2
0.0938	0.999
0.0924	0.9988
0.0956	0.9992
Pool Fire	
Mass Loss Rate (kg/s)	R^2
0.094	0.9988
0.0935	0.999
0.0933	0.9922
% Difference in Averages	-0.4%

2.1.1.2. Final Test Apparatus and Wick Design:

The final wick stand, shown in Figure 8, was primarily constructed of one inch, 80/20, T-slot aluminum. The stand held the wick between 10 and 16 inches from the working surface, depending on the orientation, and was capable of holding different wicks via steel clamps that were tightened with bolts. The horizontal arm that held the clamp is constructed of an eighth-inch thick “L” shaped aluminum beam that was shielded with *Kaowool 3000* board and sheet metal to protect wires or water tubes that need to reach the clamp. Later an additional “hanging clamp” was added below the wick clamp to help support and hold the heat flux sensor in position.

Testing wicks utilize a half-inch backing of *Kaowool 3000* board that helped to minimize heat leaving the burning area, as well as prevent heat from reentering through the rear of the wick – particularly when burning in the ceiling orientation. Aluminum foil was adhered to the top of the backing with a combination of sodium silicate, silicone sealant, and epoxy. Sodium silicate was then used as an adhesive to attach the top layer which is constructed of 0.32 cm *Kaowool PM* board. The desired saturation area is the

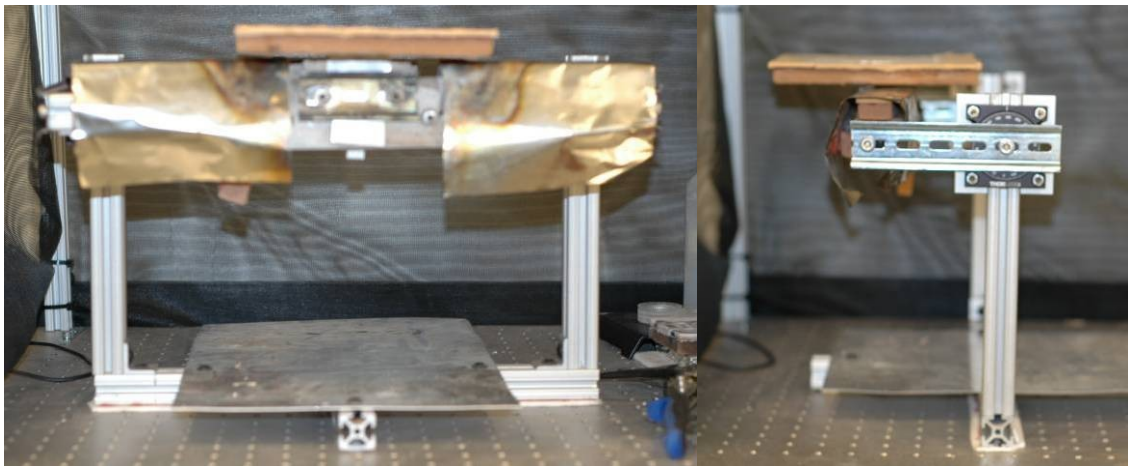


Figure 8. Front and side views of liquid wick stand, with clamped in wick.

same material as the surrounding border but separated from it by an aluminum foil wrapping. Particularly with the round wicks used in microgravity testing, some problems with the fuel leaking through corners or rounded areas was observed and rectified by first coating the neighboring area and *Kaowool PM* edges with sodium silicate. When sodium silicate was used in a position like this where it would be exposed to fire, construction of the wick would finish with several repeated inverted burns causing the sodium silicate to intumesce as much as possible. This protruding sodium silicate would then be gently sanded off. Each wick meant for testing in normal gravity had a square piece of sheet metal affixed to the rear with an epoxy. A smaller strip bent into a “U” shape was then attached to this piece of metal backing. This fit into the clamping mechanism built into the rotating stand described above.

If the wick was being constructed for testing where heat flux readings were desired, a hole was drilled through the center of the burning region. A steel hypodermic tube measuring an inch in length (the heat flux gauge stem length) was then inserted. This was sealed and held in place by epoxy. A wick for heat flux testing can be seen in Figure 9.

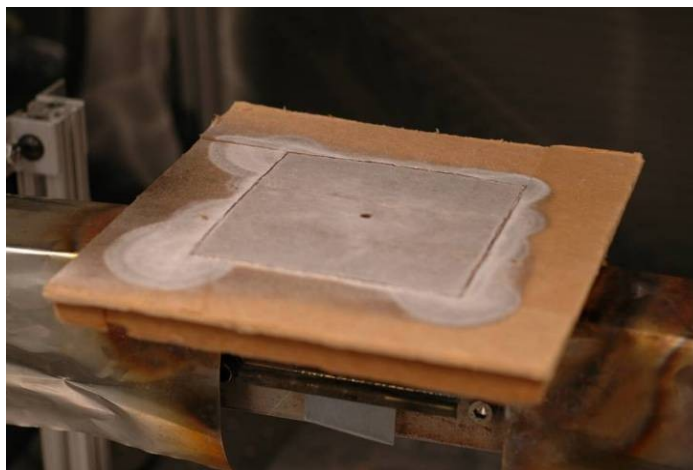


Figure 9. Liquid fuel wick measuring 10 x 10 cm. Center hole accommodation allows for the heat flux gauge to pass through and be positioned level with the surface.

2.1.1.3. Testing Set-up:

For burning rate testing the stand was placed on top of a balance interfaced with a computer. “BalanceLink” was used to communicate with the balance and record the instantaneous mass at a frequency of 1 Hz. A camera was placed approximately 1 m from the stand and aimed down the surface of the wick. A fume hood choked down to minimal flow was located above the stand, located on a track constructed of T-slot aluminum so it was capable of lateral movement. The entire track support frame was then surrounded with two layers of insect screen to help dampen and eliminate any air movement effects due to ventilation or movement within the lab area.

When heat flux readings were desired, the balance was removed since the water circulation required to cool the heat flux sensor introduced too much noise to record sensible mass values. A small tank water heater capable of raising the water temperature to 70 °C was used to prevent condensation on the gauge face. Water was run through the heater and heat flux gauge at approximately the same rate ($\pm 5\%$) for each test. A NetDAQ was used to record the heat flux. All heat flux gauges were calibrated against a gauge calibrated with a NIST-originating standard.

2.1.1.4. Test Procedure:

All wicks were baked for a minimum of 45 minutes at 140 °C before a test to drive out all water condensation from previous tests. The wicks were then allowed to cool back down to room temperature.

When testing for burning rate or heat flux the first thing done was to saturate the wick. Prior testing has shown that the wick does not need to be overflowing with fuel and

will burn at a consistent steady rate provided it is not so low on fuel that the flame is receding from the edges. Accordingly, when filling the wick exact measurements were not made of the amount of fuel being added. A wick would be loaded with fuel such that all of the pyrolysis region would be wetted, allowed to sit for 15 – 30 seconds and then was topped off before moving on to the next step.

At this point if circulating water (heat flux testing) was required it would be turned on and all recording equipment would be started as well. The wick would then be rotated to the desired angle and the screen cage would be closed. If a heat flux sensor test was being conducted sensor temperature was monitored and once 65 °C was reached the test would commence.

A butane lighter flame was then used to ignite the fuel. Since prior testing showed steady burning between 10 and 90 seconds for most tests pictures of the flame would be taken 30 to 60 seconds after ignition. Wicks allowed to burn till all the fuel had been consumed.

When flame shapes were being analyzed the pictures were first imported into Paint.NET and a grid overlaid on the photograph so that measurements could be taken at consistent lengths. Measurements started at where the flame was anchored to the wick and were taken every 0.25 cm at the furthest point from the wick where the flame is observed. All measurements were taken using the graph digitizer program “GraphClick”. The results from a minimum of five photographs could then be averaged at each given distance and compiled to arrive at an “average flame height” contour for each given orientation if desired.

The following, Figure 10, shows the testing set-up.

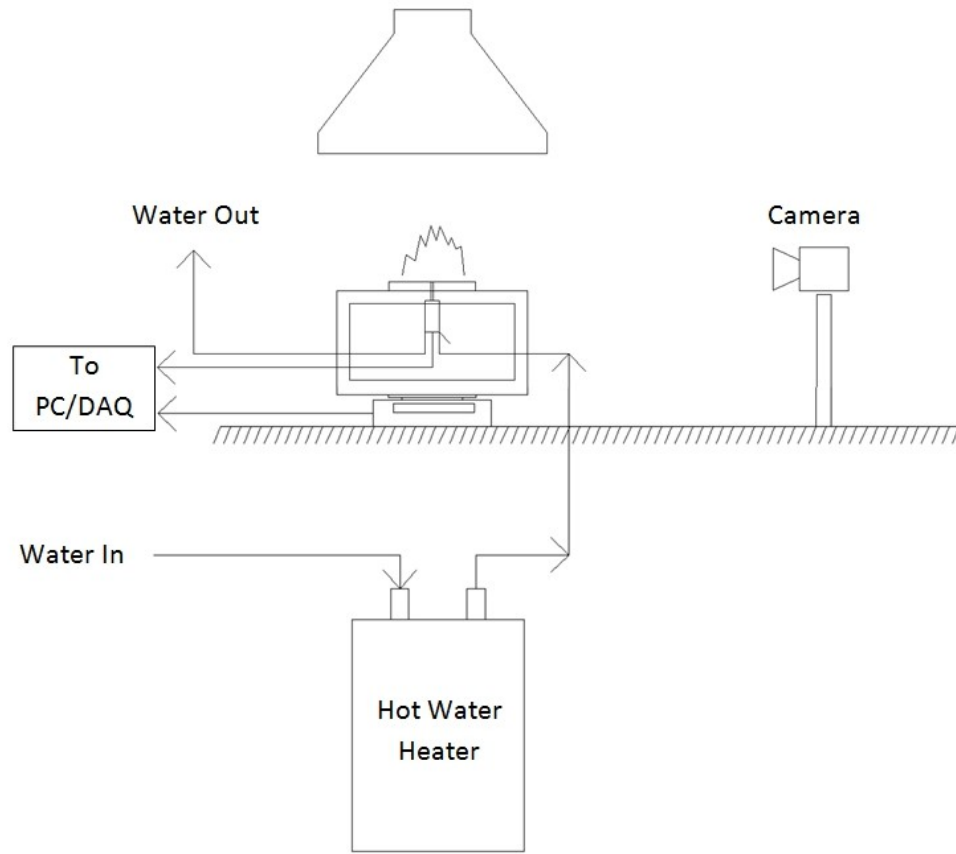


Figure 10. Testing set-up for 1g burning rate, liquid fuel wicks. Nikon D70 is used to take the still images.

2.1.1.5. 1g Liquid Fuel Test Matrix:

In order to characterize gravitational effects through the full range of possible angles ($+90^\circ$ to -90°) and based on the availability of comparable data in the literature, it was decided that testing would be conducted every 30° . Additionally, two “ideal” fuels – Methanol and Ethanol, relatively clean burning alcohols – were chosen so the eventual calibration of the BRE could be conducted for multiple fuels without introducing too many complicating factors. Since the combustion reaction involving these fuels primarily releases carbon dioxide and water vapor, as well as a minimal amount of soot, this also

enables the repeated use of wicks with confidence that the radiative and conductive properties remain relatively constant from one test to the next.

As shown in Blackshear and Murty [5], the burning rate of a flat sample where convection is the controlling mechanism approaches an approximately constant behavior at approximately 10 cm in length. At this length the edge effects, where burning rate is significantly higher, are no longer large enough in terms of area to have a noticeable impact on the average burning rate. As such samples ranging from 1 – 10 cm should be sufficient to adequately characterize all convection dominated burning scenarios. Wicks 10 cm wide and 1, 2, 3, 4, 6, 8, and 10 cm in length were constructed for burning rate testing. Only wicks 10 cm in width and 10 cm in length were constructed for heat flux testing. These desired testing scenarios are shown in Table 3.

In the case of heat flux, there were a few limited cases of unusual behavior observed during a test. If this was significantly different from accompanying tests it was assumed to be due to an outside influencing factor and discarded. These cases were when there was not just a slight difference seen from one test to the next, typically these tests would lie well outside of the typically observed variation and sometimes also follow completely different trends from what was the observed standard. These were eliminated based on the premise of being possible scenarios were condensation could have affected the readings, provided the water temperature dropped fast enough to allow it, since similar behavior was also seen to a greater extent when 20 °C water was being used to cool the heat flux gauge.

Table 3: 1g Liquid Fuel Test Matrix

Test Set-Up	Fuel	Wick Length (w=10cm)	Test Orientations
Burning Rate	Methanol	1, 2, 3, 4, 6, 8, 10	+90°, +60°, +30°, 0°, -30°, -60°, -90
Flame Stand-off	Methanol	10	+90°, +60°, +30°, 0°, -30°, -60°, -90°
Heat Flux	Methanol	10	+90°, +60°, +30°, 0°, -30°, -60°, -90°
Burning Rate	Ethanol	1, 2, 3, 4, 6, 8, 10	+90°, +60°, +30°, 0°, -30°, -60°, -90

2.1.2. Gas Burner Tests

2.1.2.1. 1st Prototype Design:

The first gas burner prototype was designed and constructed with the purpose of testing construction methods and conducting basic emulation attempts of the 10 x 10 cm methanol wick results. To keep the design simpler the heat flux sensor and surface cooling tubes were omitted, and readily available materials were used for construction when possible. This prototype was constructed out of a stainless steel box measuring approximately 13 cm x 13 cm x 4 cm, see Figure 11. A Swagelok quarter inch union, which serves as the fuel inlet, was attached to the middle of the bottom of the box. All corners of the box and the fuel port were sealed with a fire-resistant sealant to prevent leaking. A steel baffle with 0.3 cm holes is located 0.6 centimeters above the inlet and helped to spread out the fuel after injection. Above the baffle 2.5 cm of glass beads incased in two layers of aluminum insect screen further helped to evenly distribute the fuel across the entire surface of the burner. The burner is topped off with a 2.5 cm ceramic honeycomb plate with 2 mm holes. The edges of the burner and the protruding ceramic are also sealed with the fire-resistant sealant.

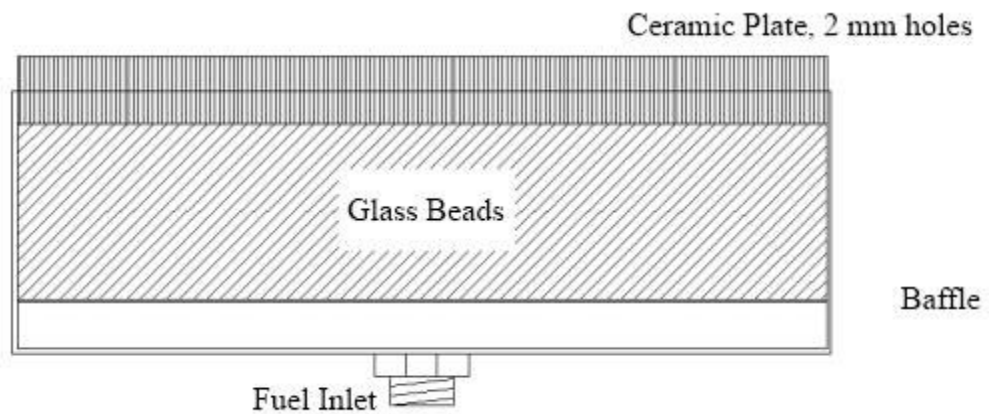


Figure 11. First gas burner prototype schematic.

The burner was limited down to a 10 x 10 cm burning area by securing a sheet metal plate with the desired pyrolysis area cut out of it to the front face of the burner. This was lined up with the bottom edge of the burner. Testing showed that this would bow outwards almost immediately so an additional metal strip measuring approximately one millimeter thick was clamped across the top and sides. *Kaowool PM*, 6.4 mm thick, was then attached to all surrounding sides to insure similar flow to the liquid-fueled wicks.

The stand was constructed out of 80/20 extruded T-slot aluminum and capable of being oriented at all angles without interrupting the side line-of-sight for the camera. The burner was secured at any given angle by tightening bolts that passed through the pivot points.

2.1.2.2 1st Prototype Testing Set-up:

The prototype was set up in the same positioning as the liquid wick apparatus. The entire testing area was again surrounded with two layers of insect screening and the exhaust vent choked down to a minimal amount of flow. The camera was set-up to aim down the surface of the wick at approximately the same distance from the leading edge of the flame. The stand was placed such that the flame side faced away from the nearest wall and approximately centered between the two sides of the screen “cage”.

2.1.2.3. 1st Prototype Test Procedure:

Methane fuel flowed through the burner at a mass flow rate equal to the measured mass loss rate of the same size liquid wicks at each given orientation. The fuel flow

would initially be set at a minimal rate required to establish a flame. The fuel would be ignited, the rate increased to the required rate for the given orientation being tested, and then photos taken as quickly as possible. Photographs were taken between 5 and 15 seconds after ignition of the burner in order to minimize temperature rise of the surface. Using an infrared thermometer the temperature of the surface was measured at the conclusion of testing with a maximum value of 175°C observed.

2.1.2.4. 2nd Prototype Design:

A second prototype was designed and constructed towards the conclusion of this thesis work, see Figure 12. During work with the first prototype, the end focus of the project was shifted from testing primarily on the airplane at different levels of partial gravity to testing on the space station. With the new focus being exclusively 0g testing,

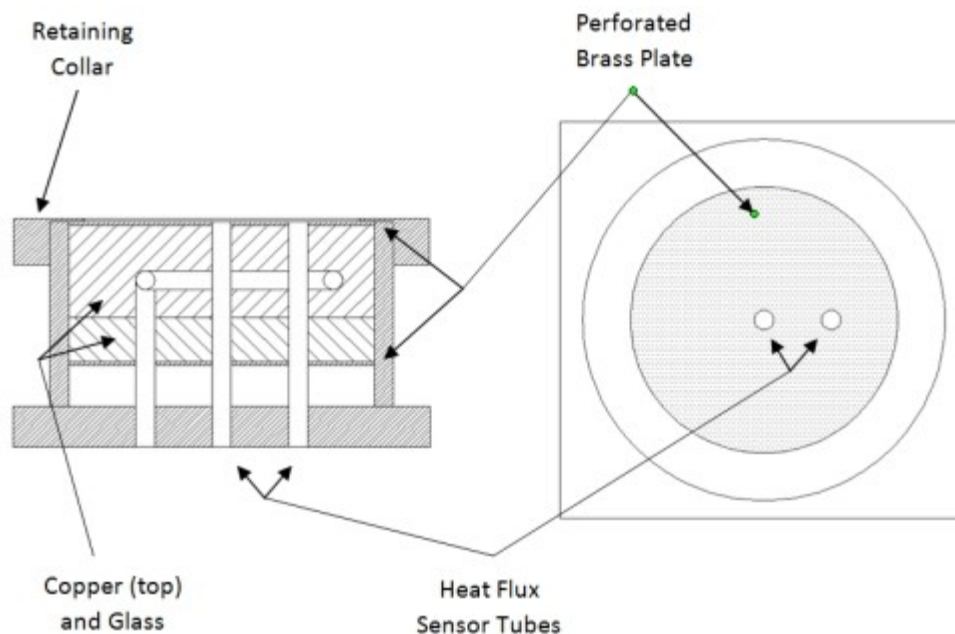


Figure 12. Schematic of second gas burner prototype.

the concentration on a rectangular pyrolysis area, which was chosen to observe the gravitational effects at different orientations, was abandoned for an axisymmetric pyrolysis area.

The new prototype's pyrolysis area measures 5 cm in diameter and includes both surface cooling tubes and accommodations for two heat flux sensors. The smaller size was chosen for its reduced oxygen consumption and will allow for longer burning times on the space station. The surface of the burner is a perforated brass plate with a hole diameter of 0.1 cm, and 45% open area.

2.1.2.5. 1g Gas Fuel Test Matrix:

For the first prototype it was decided to focus on one fuel's results – methanol – since the design was rudimentary and not meant to be a final design, only a learning tool to refine the end result. The only data of concern was the flame stand-off distance due to the absence of heat flux sensors. Table 4 provides a summary of the emulated flames.

Tests were run at all seven angles, and five photographs analyzed.

Table 4. 1g Gas Fuel Test Matrix

Gas Fuel	Emulated Test	Mass Loss Rate (g/m²-s)
Methane	Methanol, +90°, 10 x 10 cm	14.00
Methane	Methanol, +60°, 10 x 10 cm	14.80
Methane	Methanol, +30°, 10 x 10 cm	15.10
Methane	Methanol, 0°, 10 x 10 cm	14.77
Methane	Methanol, -30°, 10 x 10 cm	13.88
Methane	Methanol, -60°, 10 x 10 cm	12.34
Methane	Methanol, -90°, 10 x 10 cm	10.80

2.2. Experimental Results and Discussion

2.2.1. Flame Stand-off Distance Measurements:

Figure 13 shows flame images for 7 wick and burner orientations separated by 30° increments. Laminar flow was observed near the wick surface for all cases. However, turbulent flaming plumes rapidly formed above this laminar region, most notably for orientations of $0 - 90^\circ$ and lengths 6 cm or greater, see Figure 14. For wicks of 6 cm and longer in the vertical orientation an unsteady oscillating behavior was observed over the later portion of the laminar section of the flame due to the downstream turbulence.



Figure 13. Enhanced color images of flames fueled by methanol on 10 x 10 cm wicks (top) and methane through a 10 x 10 cm burner (bottom).

For $+60^\circ$ and $+30^\circ$ orientations, a boundary layer flame forms in the region immediately after the leading edge of the wick, but downstream a turbulent flame forms and is pulled away from the wick due to buoyancy. Methane burner flames exhibited turbulent behavior earlier than methanol flames and had much larger over-fire regions. The over-fire region is not shown in the figure. This difference in the over-fire region where a turbulent flame occurs is due to the differences in the heat of the combustions between the methanol and methane (discussed in Burner Rationale section).

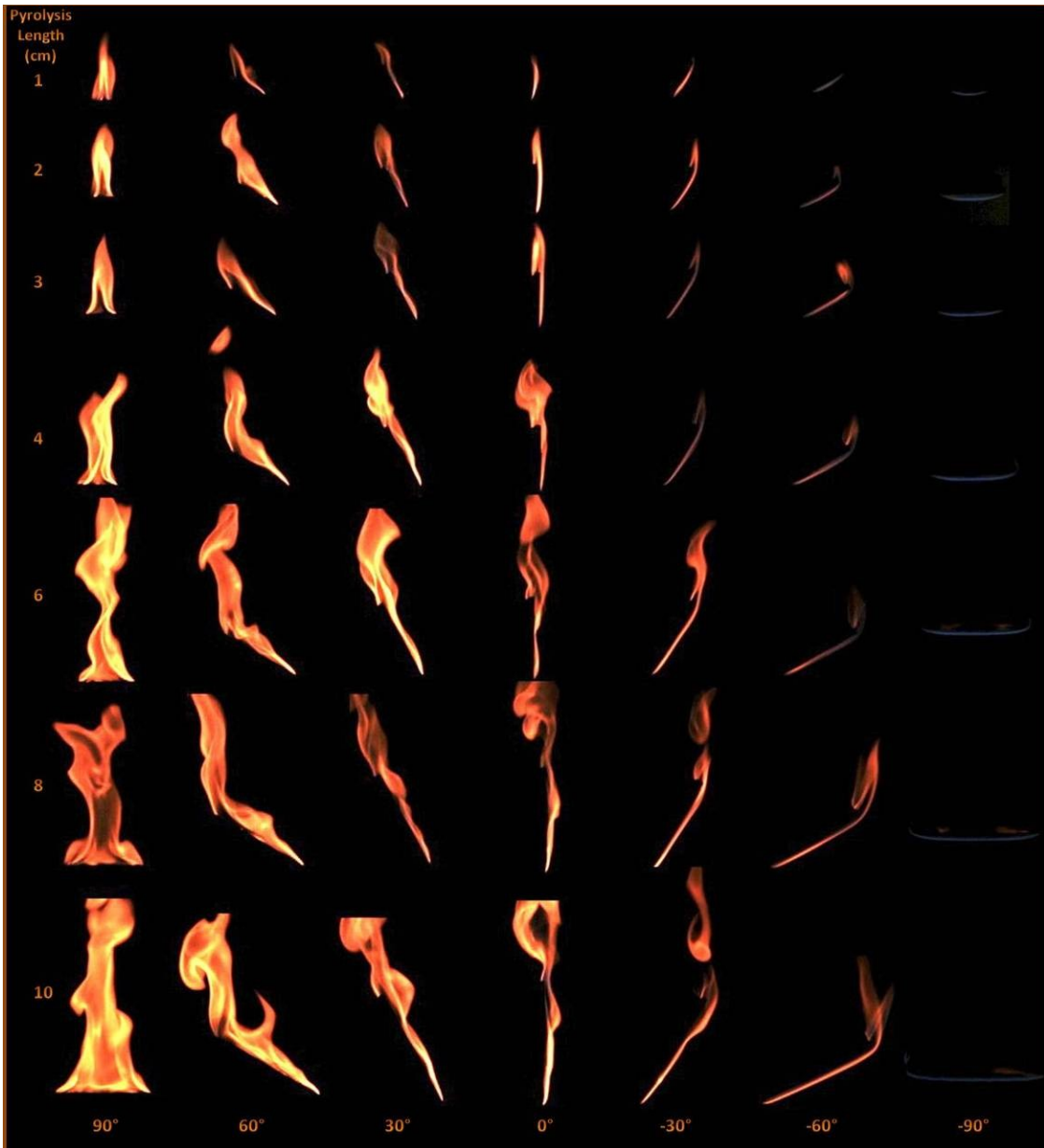


Figure 14. Snap shots of flames fueled by methanol for all sizes and orientations.

During burning, the flames were initially weak and dim upon ignition. However, the flames quickly grew and became more luminous within 5 s. Flame shapes were measured from images. Two examples from 10 cm x 10 cm methanol and methane tests are presented in Figure 15, and compared to the model results, with and without the cross-flow effect. These results reflect laminar [typical steady] flames, and approximate

locations where unsteady behavior (U, see Appendix D for additional info on onset of unsteadiness), in the form of an oscillation or turbulence was beginning. Ali et al. [4] provides a DNS solution for similar circumstances but only for the first 1 cm. In general those results agree well in the limited section but are slightly lower for $+60^\circ$ before improving thereafter. Ali et al.'s results have also been included where available.

The methanol flame and the burner flame generally exhibit the same shape and behavior. The methane flame standoff is slightly lower for $+0^\circ$ to $+60^\circ$ and slightly higher for -30° to -90° . Both flames generally indicate the onset of unsteady flow and turbulence at the same point for a corresponding orientation. The laminar steady model predicts higher than the data, and the solution including the cross-flow (CF) show some small differences with the exact solution without CF for angles of $+60^\circ$ and $+30^\circ$.

Methanol and ethanol flames became brighter and more yellow/orange in orientations that exhibited more unsteady behavior.

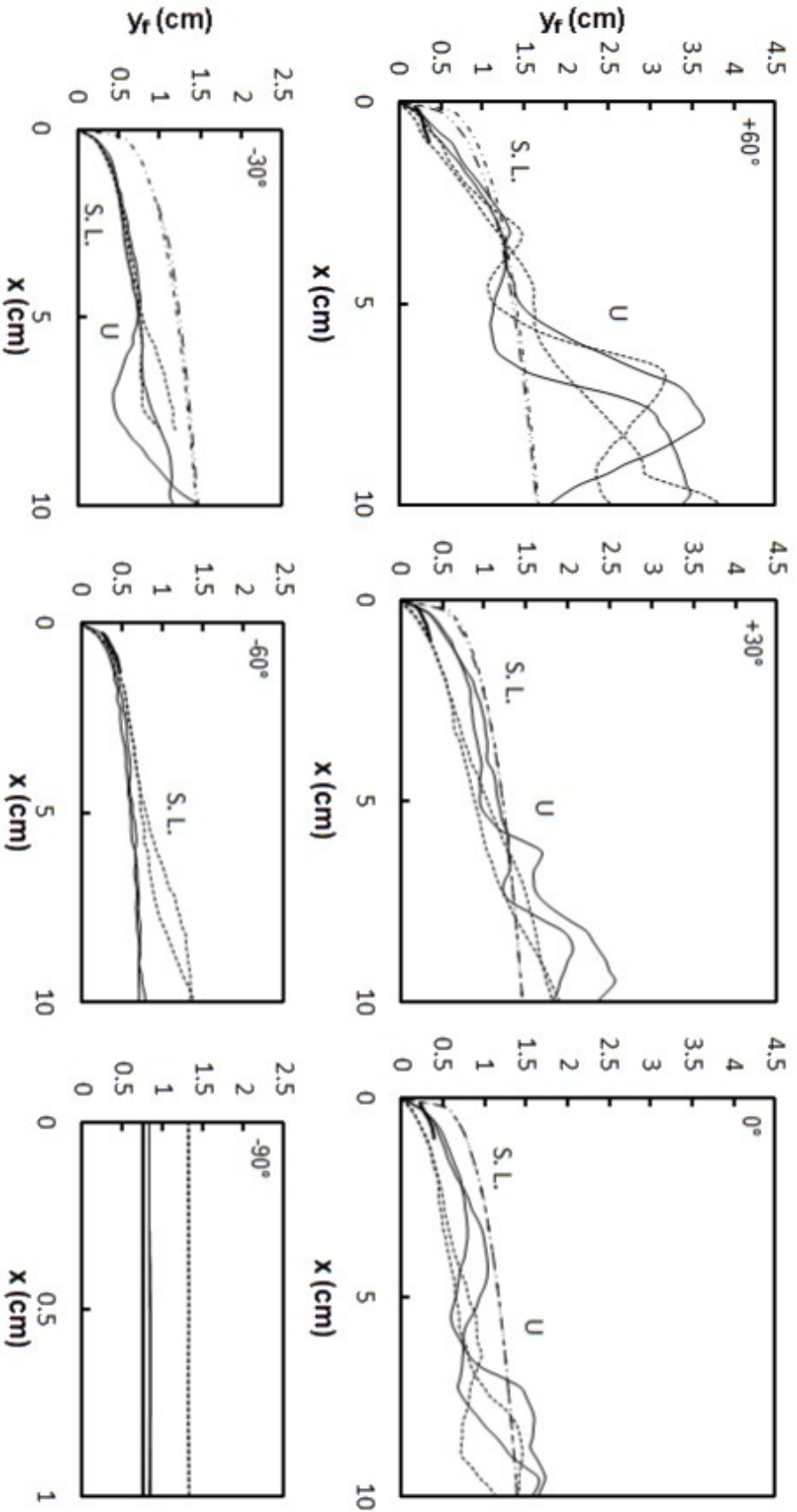


Figure 15. Measured flame heights examples from various tests at all orientations. Approximate areas where steady laminar (S.L.) and unsteady (U) behavior was observed are labeled. Methane flames simulated methanol wicks. Methanol model results with and without the cross-flow (CF) effects and Ali et al.'s [41] DNS results are included

2.2.2. Burning Rate Measurements:

Average mass fluxes for 1, 4, and 10 cm wicks at all orientations are shown in Figure 16. The maximum burning rate was observed at $+30^\circ$, a result in agreement with Blackshear and Murty [6]. As wick length decreased the amount of variation seen with angle also decreased.

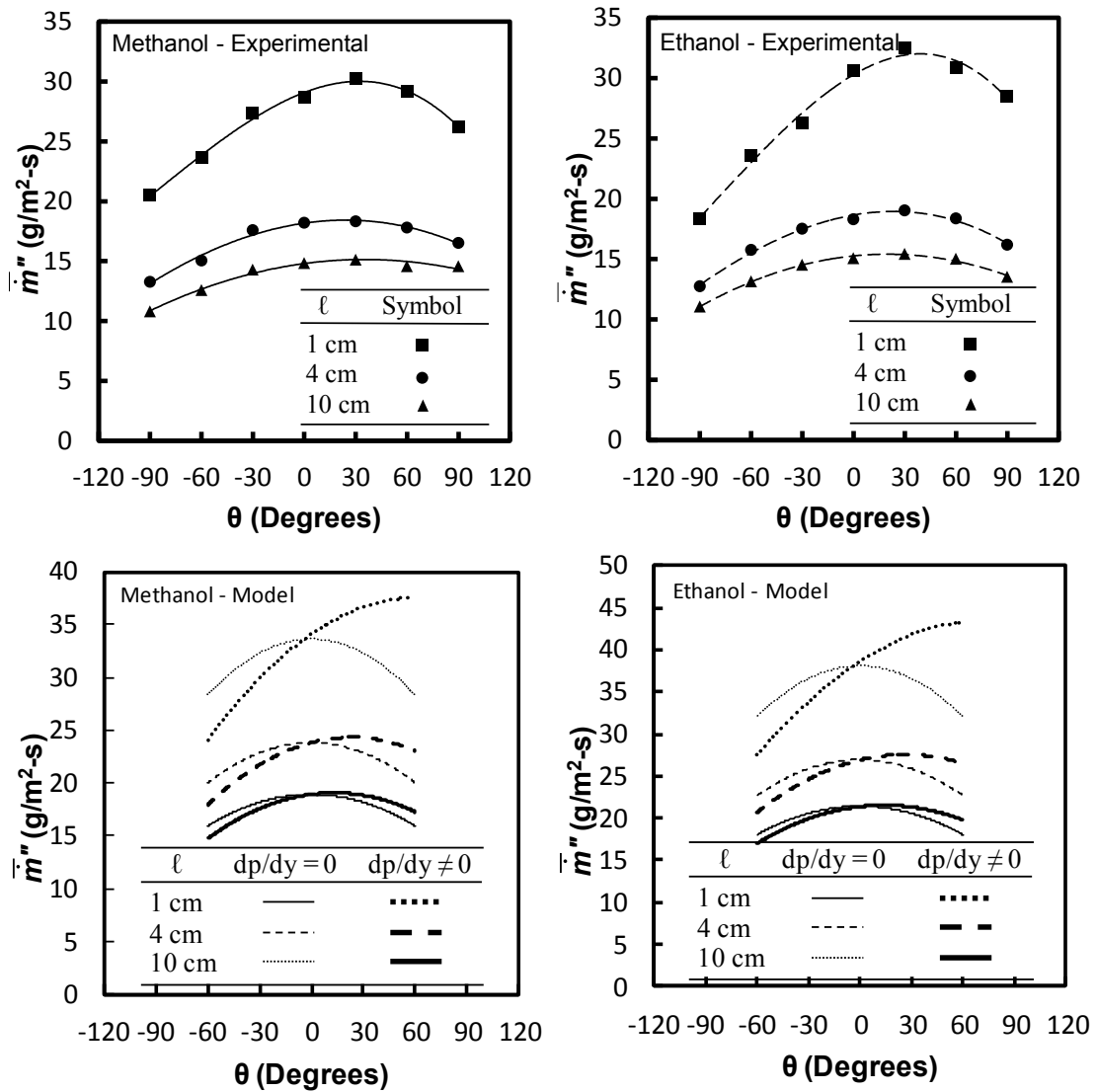


Figure 16. Average mass flux of methanol and ethanol as a function of angle for wick lengths of 1, 4, and 10 cm at angles ranging from -90° to $+90^\circ$. Experimental (top) and model (bottom) results are included.

For methanol testing on the 10 x 10 cm wick, the burning rate measured at +60° and +90° approaches that of the maximum at +30°. This suggests that if the wick length was extended even further a new maximum may arise at the pool fire orientation, +90°. This result would be in agreement with more turbulent tests such as [8].

Model results excluding cross-flow effect predict a maximum burning rate in the vertical orientation, a predictable outcome as it does not account for burning on top and bottom. Excluding the shifted maximum, these predictions still qualitatively appear to be favorable. On the other hand, the model results fail to quantitatively capture the behavior as it over-predicts in almost all cases by 15 – 40%.

When including the cross-flow effect the model begins to capture the shift in the maximum. This is an exciting qualitative result as the inclusion of this extra term clearly has a dramatic impact here despite a minimal effect on the flame stand-off predictions. Moreover, by capturing the burning behavior, with respect to top or bottom burning, the model recognizes that the maximum is not at the vertical orientation and even correctly predicts in which direction the maximum should shift. Unfortunately, the model still falls short of being quantitatively accurate as discrepancies still typically range from approximately 15 - 40%, like the previous model, but with smaller variations seen in the negative angles and larger variations seen in the positive angles. These differences are likely due mostly to the combination of what property values were chosen and the lack of inclusion of the flame radiation losses.

Seen in Figure 17, wick burning rates for both methanol and ethanol fuels converge with increasing length in agreement with the results of [5]. The model does better for the small lengths, as these remain laminar while the longer lengths, typically

above 5 cm from Figures 13 and 14, are worse. Of course this poorer agreement is understandable as the model cannot deal with the onset of turbulence and possible radiation effects in a thicker boundary layer. While the model with CF can show some distinction with top and bottom flame orientations (Figure 15), the original model of Ahmad and Faeth [3] (without the CF) cannot.

Figure 18 shows the measured normalized burning rates plotted as a function of a modified Rayleigh number as developed by Ahmad and Faeth [3]. Despite the differences between model and data in the previous figures, the log-log correlation looks very and good, and our data are consistent with theirs.

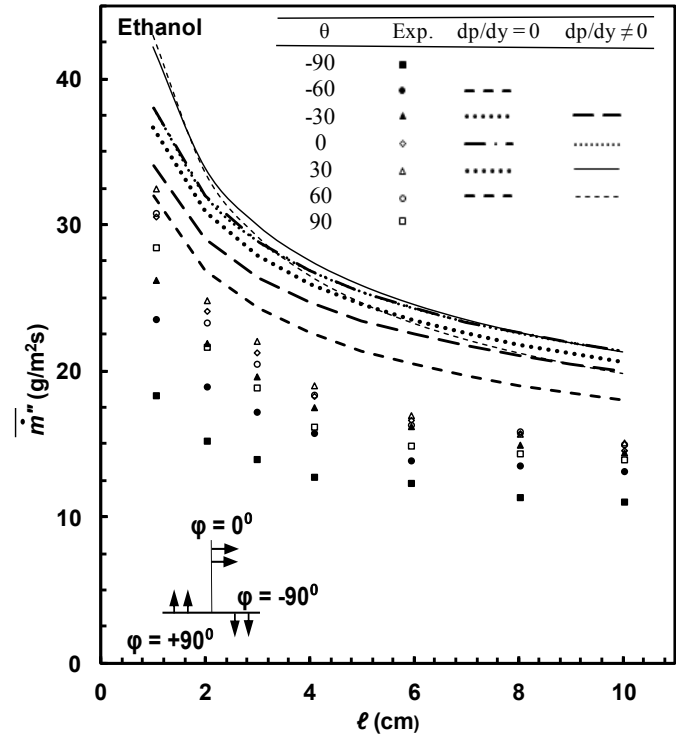
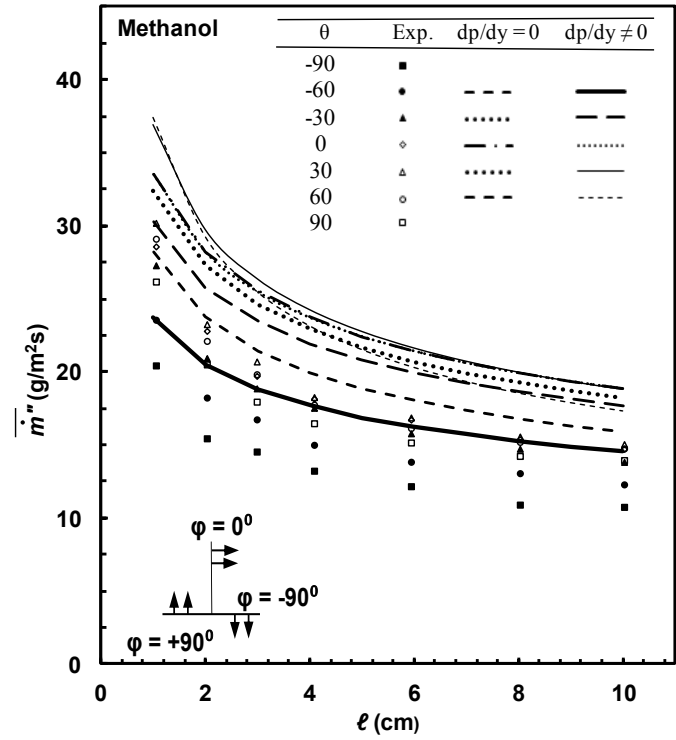


Figure 17. Average mass flux from model and experimental results of methanol and ethanol for wick lengths of 1, 2, 3, 4, 6, 8, and 10 cm at angles from -90° to $+90^\circ$. Model results including the CF effect ($dp/dy \neq 0$) and excluding the CF effect ($dp/dy = 0$) have been included.

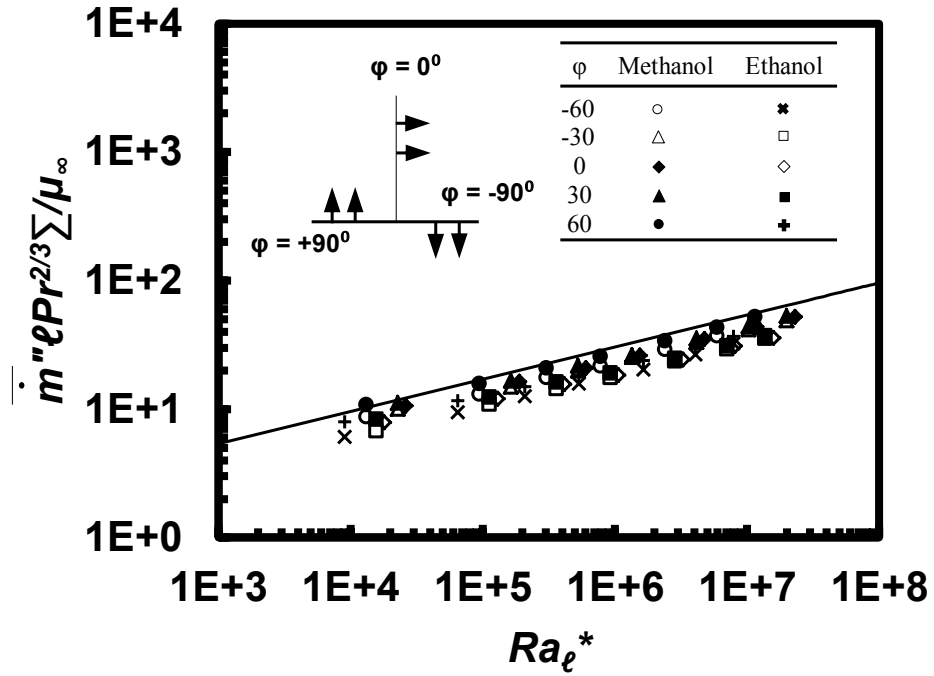


Figure 18. Burning rates of methanol and ethanol plotted with respect to the modified Raleigh number with the orientation angle correction. The line is the theory of Ahmad and Faeth [3]. The chosen property values for calculations are shown in Table 1.

2.2.3. Heat Flux Measurements:

As expected, heat flux measurements taken at the center of the pyrolysis region, Figure 19, followed the same trend for angles -90° to $+30^\circ$ as the recorded burning rate measurements. However this trend deviates for $+60^\circ$ and $+90^\circ$, this is expected based on the setup as the flame displays more prominent separation from the wick as buoyancy pulls the flame up and away from the surface. The integral model results compare favorably with measured values at the given location. However, as also noticeable when looking at the burning rate in Figure 16, the predicted maximum differs from the experimental. The agreement we believe is fortuitous, as previous results for the flame stand-off and mass flux were over predicted by the model. The model can only predict convective heating and we believe the agreement is due to radiation from the flames and an over prediction in the convective flux.

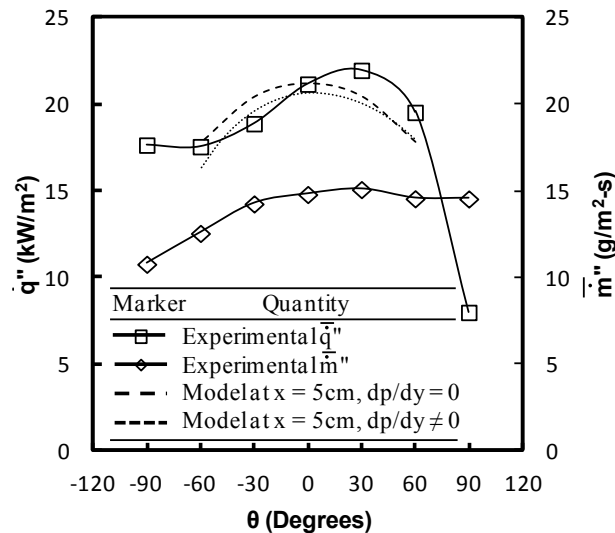


Figure 19. Local heat flux and average burning rate measured at $x = 5$ cm for Methanol soaked wicks, and at angles ranging from -90° to $+90^\circ$. Numerical results for the integral analysis are also included.

3. 0g Testing

3.1. Experimental Set-up and Procedure

3.1.1. 0g Airplane Tests

3.1.1.1. Simulating Microgravity with an Airplane:

One method for testing at different gravity levels is to load the project on to an airplane and fly in a parabolic path, as shown in Figure 20. When flying over the crest of a parabola the downwards acceleration of the plane has an opposite effect on the passengers and contents of the airplane resulting in reduced gravity levels. Based on how quickly the plane is accelerating through the parabola different gravity levels can be achieved. This method of testing enables researchers to conduct longer duration microgravity testing then might be provided by a drop tower, on the other hand this also has the inherent disadvantage of being exposed to “g-jitter” – a term used to reference the small amount of turbulence effecting the gravity level at any given time.

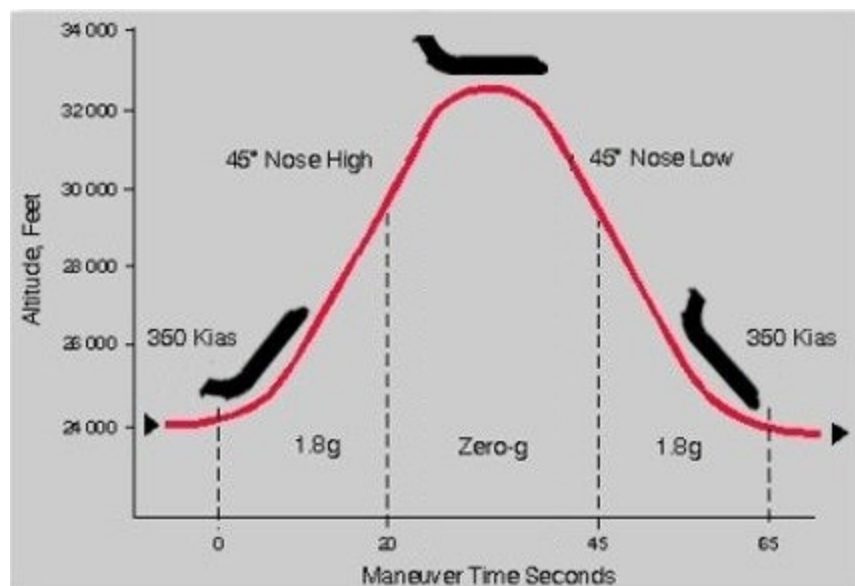


Figure 20. Flight path of airplane for 0g testing, from [18]

3.1.1.2. Test Apparatus and Wick Design:

For 0g testing on the airplane the desired requirements were supplied to NASA – Glenn Research Center who hired Sierra Lobo, Inc. to design and construct the testing apparatus.

For airplane testing there were several new safety and operation concerns. First and foremost, in the extreme case that the fuel had time to entirely evaporate within the chamber, the atmosphere must not reach the lower explosive limit of the fuel (ethanol). Based on the volume of the chamber this was calculated to be just over two grams of fuel.

Another initial concern was oxygen consumption. It was decided that oxygen concentration with-in the chamber should only be allowed to decrease to a minimum of 19%. Using the maximum recorded mass loss rate during 1g testing, a worse-case scenario burn time required to reach this oxygen level was calculated to be approximately 40 seconds. This concern was consequently dismissed since 0g parabolas only last around 20 seconds. It should also be noted that the burn time calculations should provide a conservative estimate as burning in microgravity has been shown to be less vigorous due to the lack of buoyant flow [17], which would serve to decrease the rate of oxygen consumption as well.

The airplane rig is designed to accommodate a wick of overall dimensions 11.4 x 11.4 x 1.6 cm. The wick is secured into a tray with set-screws that drill into the four corners of the bottom insulation layer. A cover plate, which is actuated by an air-driven cylinder, covers the wick and rotates up 85° when testing. A wire-igniter, also controlled by an air-driven cylinder, can rotate down from the edge of the tray into the center of the

wick to start a test. The entire tray assembly pivots around its center and is capable of locking into its position every thirty degrees.

The testing chamber is a steel 27L chamber, see Figure 21, with viewing windows through its front and side. Two cigar cameras are incorporated the rig: one that points through a chamber window and down the axis of rotation of the tray, the second camera is inside the chamber and is pointed at a mirror mounted on the lid to record the top view of the wick.



Figure 21. Aircraft rig with testing chamber seen on right. Window provides view down the top of the wick.

A data acquisition system records temperature, pressure, and g-level. The temperature is recorded by a pair of thermocouples, one located by the lid and the second located on the underside of the tray. The pressure is recorded both inside and outside of the chamber, and the g-level is recorded by plugging into the airplane accelerometer.

The chamber has three different solenoids for controlling airflow. The first solenoid opens the chamber to a compressed-air cylinder onboard that is used to restore

the chamber to standard atmospheric conditions (approximately 21% oxygen and 14.7 psia). The second solenoid opens to outside the plane and is used for venting the combustion products after a test. Lastly, the third solenoid opens to the airplane cabin and is used to flush out the chamber after it has dropped below the cabin pressure. All aspects of the chamber and its contents are controlled via a touch screen interface connected to a PLC controller.

For airplane testing rectangular wicks with a pyrolysis region measuring 1 x 4 cm were used. The rectangular shape was chosen to maintain a comparison with the collected results at the time – similar scenarios consisting of both 1g testing with rectangular pyrolysis areas measuring 1 x 10 cm and two 5.2 second drop tower tests also utilizing a 1 x 4 cm pyrolysis area wick.

Wick construction techniques and materials for the smaller wicks were kept the same to make the results as comparable as possible. Dimensions of the overall top surface of the wick are 11.4 x 11.4 cm and the pyrolysis area - located in the center - for all airplane tests measured 1 x 4 cm.

3.1.1.3. Test Procedure:

For airplane testing, all wicks were loaded with fuel prior to take off and stored in Ziploc bags. For take-off and landing the chamber solenoid to the cabin of the airplane is opened.

Once reaching the testing area, a wick is pressed into the tray, the set screws tightened, and the tray cover closed to minimize any evaporation. The chamber-to-cabin

solenoid is then closed, and the chamber lid sealed. The chamber is pressurized to 14.5 – 14.7 psi using the attached compressed air bottle.

When the desired gravity level is reached, the tray cover is rotated up, the igniter moved into position, the igniter powered, and then the igniter retracted. At the completion of the parabola the cover is closed to extinguish the flame. The chamber-to-outside solenoid is opened to evacuate any combustion products to the exterior of the airplane. After the pressure has dropped below cabin pressure the solenoid-to-cabin solenoid is also opened for approximately a minute to allow the chamber to “flush” out any lingering combustion products. The chamber-to-outside solenoid is then closed.

If a new wick is needed, at this point the chamber can be safely opened, the old wick removed, and a new wick screwed into position. The chamber is then repressurized and the test process repeated.

Testing was conducted on two separate days and during actual testing several problems were encountered. Most notable, issues were encountered with both cameras built into the testing rig. The first day of testing both cameras failed to record correctly after suffering connectivity issues, and on the second day of testing only the side view camera could be restarted after suffering from the same problem. In addition, upon examination of the footage after testing was completed, it was discovered that the flame was not visible to the camera during the parabolas. Since problems were encountered the first day, as a backup measure a person camera was held up to the front window to record all tests as well. Consequently footage of the flames is available but the view is from the front operator window and sometimes the camera itself is unsteady.

In addition to camera issues, the rig also suffered from a still unidentified issue with the accelerometer. As a result the channel for the accelerometer on the data acquisition system recorded an over-saturated signal for the duration of all the tests.

3.1.1.4. Airplane Test Matrix:

In preparation for airplane testing, two drop tower tests were performed in advance. Accordingly, one of the primary goals for the airplane testing was to try to reproduce the observed drop tower results – to hopefully prove that the g-Jitter has a minor effect.

In addition, the goal of airplane testing was to complete as many burns as possible within the given time frame in order to establish as large a database as possible to compare future gas burner tests against. Ethanol fuel was used, just as in all drop tower tests, for the reduced evaporation rate and likely brighter flames. Testing conditions can be seen in Table 5.

Table 5. 0g Liquid Fuel Airplane Test Matrix

Gravity level (g)	Fuel	Wick design	Orientation with respect to acting gravity*	Ignition timing
0	Ethanol	1 x 4 cm	n/a	Approximately 2-3 seconds before entering 0g
0	Ethanol	1 x 4 cm	n/a	In 0g
0.17 (Lunar)	Ethanol	1 x 4 cm	0	In 0.17g
0.38 (Martian)	Ethanol	1 x 4 cm	0	In 0.38g

3.1.2. Drop Tower Experimental Set-up and Procedure

3.1.2.1. Simulating Microgravity with a Drop Tower:

Another method for simulating microgravity is utilizing full or partial free fall within a drop tower. Specifically one facility, shown in Figure 22, that utilizes this method to simulate near-0 gravity is NASA Glenn Research Center's Zero Gravity Research (Zero-G) Facility. The Zero-G Facility houses a tower featuring a 132 m free fall distance which corresponds to 5.18 seconds of g levels below 0.0001g. The entire chamber measures 143 m in length and 6 m in width. After loading the drop vehicle into the top of the chamber, the tower is pumped down to a vacuum level of approximately 0.0001 psi in order to reduce the opposing acceleration effect due to aerodynamic drag.



Figure 22. Drop tower model showing cut-away of structure.

For this drop tower, the experiments are loaded into drop vehicles approximately one meter in diameter and four meters tall, which can then be positioned in the top of the drop tower. A pair of steel jaws in combination with a pin holds the vehicles. When the chamber has been brought down to vacuum and testing is ready the pin is broken with a hydraulic cylinder opening the jaws and releasing the vehicle. The vehicle lands in a deceleration cart filled with expanded polystyrene and exposed to a peak deceleration rate of 65g. The drop vehicle can be seen in Figure 23 being loaded into position.



Figure 23. Drop tower vehicle being loaded into the top of the steel vacuum chamber. After positioning the vehicle a steel cap is then lifted into place [8].

3.1.2.2. Test Apparatus and Wick Design:

The wick holding and ignition apparatus was incorporated into a pre-existing centrifuge drop vehicle. With the amount of time it takes to prep the chamber fully, about 75 minutes, excessive evaporation is a concern so the holder also incorporates a cover

plate that rests over the soaked region of the wick until the chamber is ready for testing. Additionally this cover plate is also programmed to return to this position after completion of the drop to extinguish the flame in the event that it survives.

A Kanthal resistance heating wire serves as an igniter. The ignition source can operate under manual or automatic controls. Both devices can be seen in Figure 24.

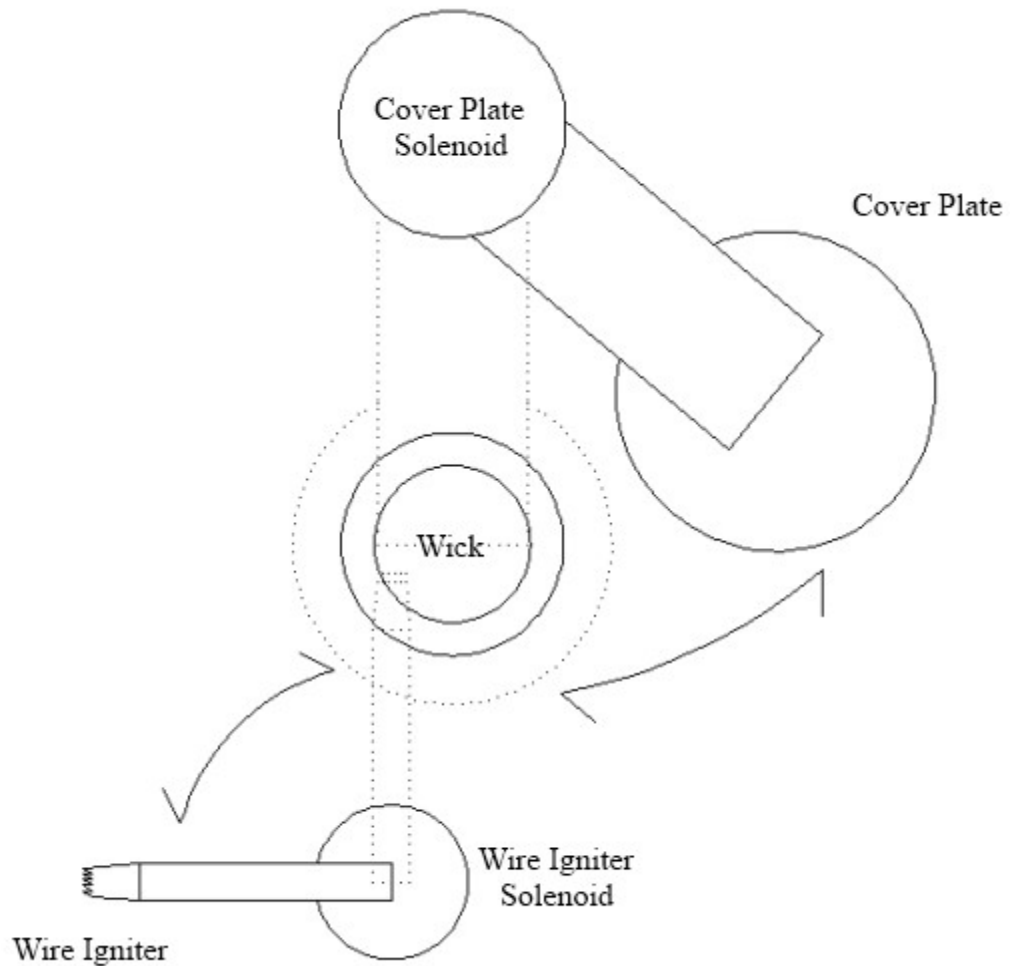


Figure 24. Layout of drop tower stand showing wick location (circular wick shown but rectangular wick's pyrolysis area would be centered in the same spot), cover plate location, and wire igniter location. Dotted lines show the movement of the cover plate and wire igniter.

Two different shape wicks were used for drop tower testing, both of which utilized the same building materials as prior wicks. Two tests were performed utilizing the same style wick flown in the airplane. The overall wick dimensions were approximately 11.4 x 11.4 x 1.6 cm, with a pyrolysis area measuring 1 x 4 cm. A second set of tests were run utilizing a wick meant to be comparable to the second gas burner prototype. These wicks featured a pyrolysis area measuring five centimeters in diameter with a border measuring approximately one centimeter in width. Like some previous wicks, these were made using *Kaowool PM*, *Kaowool 3000*, aluminum foil, sodium silicate, and epoxy.

3.1.2.3. Test Procedure:

Approximately an hour and fifteen minutes before the actual test the pyrolysis region of the wick would be loaded with fuel and the cover plate moved into position. The centrifuge chamber would then be closed.

For tests where an atmosphere differing from room conditions was desired, the chamber was then pumped down to 10 psi before refilling to a pressure above room conditions (14.5 psi). A solenoid between the chamber and the room would then be opened and while leaving the bottle filling the chamber open to flush out the chamber for fifteen minutes. As a side note: typically when replacing the atmosphere in the centrifuge chamber, NASA's procedure would be to pump to a near vacuum before refilling with the new gas however this could not be done with our experiment since this would speed the evaporation process. At the conclusion of the flushing process the solenoid and gas cylinder are closed.

The vehicle's sidewalls are then attached with quarter-turn bolts. The vehicle's top spindle is then clamped into the jaws and the entire rig lifted into position. The chamber is sealed with a cap and the vacuum process started. A five-stage process pumps the tower down to a vacuum over the course of an hour. At the completion of the pumping process, safety pins that prevent an accidental drop are pulled out of position.

The actual dropping process is initiated in the control room. If an automatic ignition sequence is being used this will also be initiated by the same control. Three different ignition methods were used over the course of the six drops. Two tests were performed with manual controls resulting in 1g burning for a period of two to three seconds. One drop was performed with an automated sequence where ignition occurred approximately a half second after drop and three automated drops were performed with ignition approximately a half second before the drop.

The ignition process starts with the removal of the cover plate. A chamber LED is then powered to insure proper removal. The igniter is then moved into position, powered, and then removed.

The drop vehicle enters free fall for 5.18 seconds before impacting the expanded polystyrene. At this time the cover plate is automatically returned to the closed position and if an enhanced atmosphere was used the solenoid between the centrifuge chamber and the drop tower was opened, evacuating the chamber and extinguishing any possible remaining flames.

3.1.2.4. Drop Tower Test Matrix:

The drop tower provides a cheaper alternative to testing in 0g conditions but is limited to a test length of 5.18 seconds. These tests also provided a much more “pure” 0g environment – in terms of far less disturbances – and were hoped to help lend credibility to the airplane testing through reproducing the results.

Since opportunities to test in the drop tower are very limited the testing plan was revised and based on the results from the previous tests as we progressed. The first two tests were before airplane testing and utilized the same style wick. After airplane testing another opportunity arose for additional testing. By this time the new gas burner prototype had been designed and built, with the revised circular pyrolysis area it was then decided to pursue testing with circular wicks. Table 6 includes testing details for all tests conducted in the drop tower.

Table 6. 0g Liquid Fuel Drop Tower Test Matrix

Gravity level (g)	Fuel	Pyrolysis area	Atmosphere	Ignition timing
0	Ethanol	1 x 4 cm	Standard ¹	~3.0 s before drop
0	Ethanol	1 x 4 cm	Standard ¹	~0.5 s after drop
0	Ethanol	2.26 cm diameter ²	Standard ¹	~3.0 s before drop
0	Ethanol	5 cm diameter	Standard ¹	~0.5 s before drop
0	Ethanol	5 cm diameter	30% oxygen, 14.7 psi	~0.5 s before drop
0	Heptane	5 cm diameter	30% oxygen, 29.4 psi	~0.5 s before drop

¹ Filled with “room” air, ~14.5 psi, 21% oxygen

² Equivalent area to 1 x 4 cm rectangle

3.2. Experimental Results and Discussion

3.2.1. Flame Shape Photographs:

A total of 14 0g flames were recorded during airplane testing and 6 0g flames during drop tower testing.

In the case of airplane testing steady elliptical flames, see Figure 25, were observed to burn for a period of 6 – 20 seconds. The burning only ceased in this scenario when manually extinguished by the closing of the cover plate.

These results are believed to be the first 0g results where a steady state condensed



Figure 25. Elliptical ethanol flame at 0-g. Burning area measures 1 cm x 4 cm, viewing 4 cm side.

fuel flame was established on a planar surface in quiescent and ambient conditions. A summary of these tests can be seen in Table 7.

An anomaly was observed during test 10 where the wick was ignited just prior to entry into 0g. For this test a spiraling flame was recorded rotating around the base of the elliptical flame. It was a curious occurrence and an example of a rotation can be seen in Figure 26.

Table 7. Ethanol Flames at 14.5 – 15.0 psi and 0-g.

Test	0-g Burning Time (s)	Notes
1	6	
2	20	
3	11	initially lifting off left side, flashes over and establishes elliptical flame
4	16	left disturbed for majority, slight buoyant effects before reverting to elliptical flame
5	18	
6	8	
7	18	
8	18	left side appears to detach mid test and reattach before parabola exit
9	17	backside of flame appears detached first 12s
10	15	ignited under buoyancy (~1s), spiraling flame base
11	20	ignited under buoyancy (~5s), steady elliptical flame
12	18	some flame movement observed during part of test
13	10	
14	20	small spark-like disturbances



Figure 26. Ethanol elliptical flame in 0-g demonstrating observed spiraling behavior around its base.

Both drop tower tests conducted prior to the airplane testing had results differing from the airplane tests. For the first drop the wick was allowed to burn for approximately three seconds before the drop vehicle was released. After release an unsteady elliptical flame was observed. Over the course of the test the one side of the flame extinguished while the opposing side slowly lifted off and away from the wick surface, behavior indicative of extinguishment. This elliptical flame exhibiting this type of behavior can be seen in Figure 27.



Figure 27. Image from first drop tower testing of an elliptical ethanol flame at 0-g. Burning area measures 1 cm x 4 cm, viewing 4 cm side.

For the second drop ignition took place in 0g. For this test a similar elliptical flame was observed but self-extinguished within 1-2 seconds.

The following four tests took place months later and utilized the same shape and size as the second prototype burner, with the exception of the first test, as mentioned previously. For these tests the wick stand was also repositioned further from the edge of the testing chamber to eliminate the possibility of that causing a disturbance. With these new tests ignition took place ~ 0.5 seconds before release to give the flame a chance to establish itself.

Elliptical flames were observed for all tests. The first three tests utilized ethanol had similar results to the prior test with ignition in 1g. The fourth test actually self-extinguished just prior to impact and the fifth test exhibited more steady behavior as a result of the increased oxygen but still exhibited clear extinguishing behavior. The last test utilizing heptanes, 30% O₂, and a 29.4 psi atmosphere resulted in a very steady and much brighter flame, see Figure 28, that grew taller over the course of the test but showed no clear extinguishing behavior. A summary of these tests are shown below in Table 8.



Figure 28. Image progression from drop tower testing of an elliptical heptane flame at 0g. Far left image is from shortly after dropping, and progresses to the right approximately every 1.2s till just before impact. Burning area is 5 cm diameter circle. Atmosphere: 30% O₂, 29.4 psi.

Overall airplane testing was not able to be reproduced with the drop tower testing. This could be due to the g-jitter present on the airplane, the magnitude of which unfortunately could not be assessed due to equipment malfunction. Struk et al. [19] studied the effects of g-jitter and extinction and recorded g-jitter having a significant effect on most of their large scale droplet tests ranging in size from 2 – 5 cm. However, in these cases large amounts of flame movement were observed, something not seen in our testing. An example of one of Struk et al.'s flames can be seen in Figure 29.

Table 8 Drop Tower Testing Summary

Fuel	Pyrolysis area	Atmosphere	Ignition timing	Burn details
Ethanol	1 x 4 cm	Standard	~3.0 s before drop	One side lifted, other slowly moved outward
Ethanol	1 x 4 cm	Standard	~0.5 s after drop	Self-extinguished after ~1 second
Ethanol	2.26 cm diameter	Standard	~3.0 s before drop	One side lifted, no noticeable movement on other side, film hard to see
Ethanol	5 cm diameter	Standard	~0.5 s before drop	Self-extinguished, flame lasting slightly longer than test 2
Ethanol	5 cm diameter	30% oxygen, 14.7 psi	~0.5 s before drop	Unsteady on one side
Heptane	5 cm diameter	30% oxygen, 29.4 psi	~0.5 s before drop	Steady edges, taller with time



Figure 29. Several images of a spherical n-decane flame subjected to different levels of g-jitter from Struk et al. [19]. Orange line represents gravity direction and magnitude, first picture ~ 20 milli-g, and the other two ~15 milli-g.

4. Conclusions

Burning rates of methanol and ethanol on flat wicks were measured at various angles with respect to gravity. A methane burner was used to emulate methanol flames by matching the flow rate to measured burning rates and theoretical predictions were made with mathematical models that did and did not include the cross-flow effect. The key findings are as follows.

1. The average burning rate per unit area was lowest for inverted horizontal wicks and highest for wicks with upward inclinations of 30° .
2. Burning rates varied from $10 - 35 \text{ g/m}^2\text{-s}$ and decreased with increasing wick length for all orientations.
3. Dimensionless correlations, using a Rayleigh number and the orientation angle, collapsed most of the data, but not for all orientations.
4. The results compared well with the vertical wick data and theory of Ahmed and Faeth [3]. An extended integral model including cross-flow buoyancy gave small differences with the original model but appears to improve the behavior of burning rate with angle.
5. Methane flames exhibited flame stand-off distances that compared favorably to those of methanol. Over the pyrolysis region the burner flame showed similar flame standoff positions, similar onset points of unsteady behavior, and similar magnitudes of unsteady behavior.
6. A laminar two-dimensional steady model could not accurately predict all features, and is unable to deal with the onset of turbulence and radiation exhibited in plates larger than 5 cm. Adding the cross-flow effect to the steady model

improved accuracy slightly by beginning to correctly indicate trends. Quantitatively the model including the cross-flow effect more accurately predicted burning rates for downward facing orientations while the model without the cross-flow effect dealt better with the upwards facing orientations; differences from experimental values were typically on the order of 15 – 40 %. A DNS model by other investigators, limited to a 1 cm long plate, appears to give good results in the very restricted region for flame stand-off distance.

7. 0g testing on the aircraft resulted in what is believed to be the first observation of steady liquid fueled flames in quiescent and ambient conditions. Results were not reproducible with the limited drop tower testing conducted. Unsteady ethanol flames were established for the duration of the drop. Possible differences could stem from g-jitter experienced on aircraft however the lack of flame movement is suspicious. Testing with heptane as a fuel at increased pressure and oxygen content yielded a steady flame that does not exhibit any clear extinction characteristics over the course of the test.
8. Using cooling water elevated above the dew point temperature is essential for accurate heat flux readings. When using room temperature water condensation results in a significant increase or decrease, depending on the nature of how it occurs, in the heat flux readings. Kaowool PM serves as an excellent wick medium as it is sufficiently dense to burn without dripping at any angle and has minimal effect on burning rate.

Appendix A: 1g Methanol Experimental Data

Table 9: 1g Methanol Experimental Data

Fuel	Orientation	Pyrolysis Length (cm)	Burning Rate (g/m ² -s)	Heat Flux (kW/m ²)
Methanol	90	1	26.22	-
	90	2	20.55	-
	90	3	18.00	-
	90	4	16.52	-
	90	6	15.20	-
	90	8	14.28	-
	90	10	13.52	8.01
	60	1	29.15	-
	60	2	22.16	-
	60	3	19.88	-
	60	4	17.80	-
	60	6	16.19	-
	60	8	15.25	-
	60	10	15.02	19.57
	30	1	30.24	-
	30	2	23.31	-
	30	3	20.75	-
	30	4	18.31	-
	30	6	16.92	-
	30	8	15.61	-
	30	10	15.43	22.00
	0	1	28.63	-
	0	2	22.85	-
	0	3	19.76	-
	0	4	18.20	-
	0	6	16.77	-
	0	8	15.44	-
	0	10	15.07	21.20
	-30	1	27.34	-
	-30	2	20.99	-
	-30	3	18.91	-
	-30	4	17.58	-
	-30	6	15.83	-
-30	8	14.78	-	
-30	10	14.53	18.92	
-60	1	23.61	-	

-60	2	18.28	-
-60	3	16.79	-
-60	4	15.05	-
-60	6	13.88	-
-60	8	13.11	-
-60	10	13.15	17.59
-90	1	20.48	-
-90	2	15.49	-
-90	3	14.58	-
-90	4	13.27	-
-90	6	12.21	-
-90	8	10.95	-
-90	10	11.06	17.68

Flame Stand-Off:

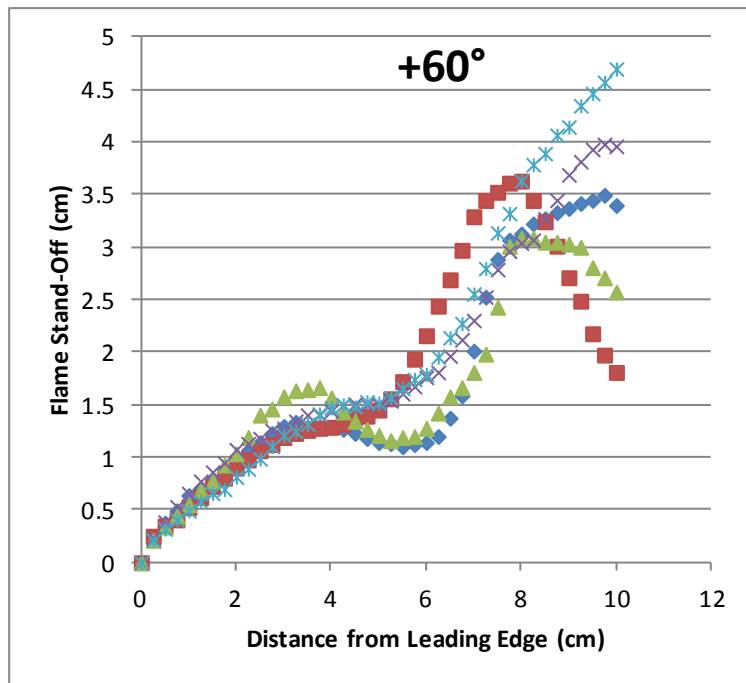


Figure 30: Methanol measured flame stand-off at +60°.

Table 10: Data for methanol measured flame stand-off at +60°.

+60 Degrees						
x	y, Image 1	y, Image 2	y, Image 3	y, Image 4	y, Image 5	y, average
0	0.2	0.2	0.2	0.2	0.2	0.2
1	0.4	0.4	0.4	0.4	0.4	0.4
2	0.6	0.6	0.6	0.6	0.6	0.6
3	1.0	1.0	1.0	1.0	1.0	1.0
4	1.5	1.5	1.5	1.5	1.5	1.5
5	1.2	1.2	1.2	1.2	1.2	1.2
6	1.5	1.5	1.5	1.5	1.5	1.5
7	2.5	2.5	2.5	2.5	2.5	2.5
8	3.5	3.5	3.5	3.5	3.5	3.5
9	3.0	3.0	3.0	3.0	3.0	3.0
10	4.5	4.5	4.5	4.5	4.5	4.5

0	0	0	0	0	0	0
0.25	0.242	0.232	0.213	0.252	0.213	0.2304
0.5	0.377	0.387	0.32	0.349	0.339	0.3544
0.75	0.494	0.532	0.407	0.407	0.445	0.457
1	0.639	0.658	0.494	0.523	0.552	0.5732
1.25	0.707	0.774	0.581	0.62	0.687	0.6738
1.5	0.774	0.862	0.659	0.726	0.774	0.759
1.75	0.871	0.949	0.697	0.804	0.929	0.85
2	0.968	1.075	0.814	0.9	1.036	0.9586
2.25	1.055	1.133	0.891	0.978	1.191	1.0496
2.5	1.142	1.181	0.988	1.065	1.404	1.156
2.75	1.229	1.259	1.104	1.123	1.462	1.2354
3	1.297	1.278	1.211	1.191	1.578	1.311
3.25	1.336	1.346	1.249	1.23	1.636	1.3594
3.5	1.287	1.404	1.317	1.259	1.646	1.3826
3.75	1.297	1.404	1.414	1.278	1.665	1.4116
4	1.287	1.443	1.472	1.288	1.568	1.4116
4.25	1.268	1.501	1.501	1.317	1.433	1.404
4.5	1.229	1.51	1.482	1.384	1.345	1.39
4.75	1.181	1.501	1.53	1.394	1.268	1.3748
5	1.142	1.501	1.52	1.452	1.21	1.365
5.25	1.132	1.539	1.569	1.559	1.161	1.392
5.5	1.103	1.607	1.656	1.723	1.191	1.456
5.75	1.123	1.675	1.743	1.936	1.2	1.5354
6	1.142	1.762	1.791	2.159	1.278	1.6264
6.25	1.2	1.81	1.956	2.44	1.423	1.7658
6.5	1.374	1.965	2.14	2.691	1.578	1.9496
6.75	1.587	2.12	2.275	2.972	1.665	2.1238
7	2.013	2.304	2.556	3.291	1.81	2.3948
7.25	2.526	2.527	2.798	3.446	1.984	2.6562
7.5	2.885	2.788	3.137	3.524	2.43	2.9528
7.75	3.069	2.963	3.321	3.611	3.01	3.1948
8	3.127	3.04	3.631	3.63	3.088	3.3032
8.25	3.223	3.069	3.786	3.446	3.088	3.3224
8.5	3.272	3.272	3.892	3.243	3.049	3.3456
8.75	3.33	3.447	4.066	3.011	3.049	3.3806
9	3.369	3.689	4.144	2.711	3.03	3.3886
9.25	3.417	3.815	4.347	2.488	3.001	3.4136
9.5	3.446	3.931	4.463	2.178	2.807	3.365
9.75	3.495	3.979	4.57	1.975	2.71	3.3458
10	3.398	3.96	4.696	1.81	2.575	3.2878

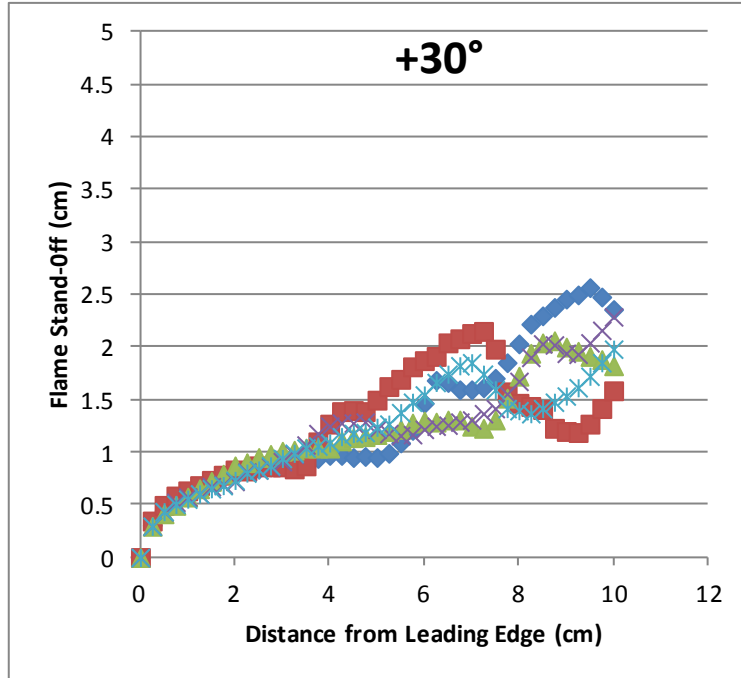


Figure 31: Data for methanol measured flame stand-off at +30°.

Table 11: Data for methanol measured flame stand-off at +30°.

x	+30 Degrees					y, average
	y, Image 1	y, Image 2	y, Image 3	y, Image 4	y, Image 5	
0	0	0	0	0	0	0
0.25	0.307	0.297	0.297	0.347	0.297	0.309
0.5	0.446	0.436	0.436	0.496	0.416	0.446
0.75	0.525	0.525	0.505	0.585	0.496	0.5272
1	0.614	0.575	0.555	0.634	0.575	0.5906
1.25	0.654	0.605	0.605	0.684	0.654	0.6404
1.5	0.714	0.674	0.654	0.734	0.724	0.7
1.75	0.763	0.694	0.684	0.783	0.793	0.7434
2	0.803	0.723	0.733	0.833	0.872	0.7928
2.25	0.842	0.813	0.803	0.823	0.902	0.8366
2.5	0.842	0.832	0.833	0.872	0.952	0.8662
2.75	0.862	0.862	0.872	0.862	0.981	0.8878
3	0.872	0.912	0.942	0.862	1.011	0.9198
3.25	0.892	0.981	0.991	0.843	1.021	0.9456
3.5	0.922	1.07	1.041	0.872	1.041	0.9892
3.75	0.942	1.179	1.06	1.1	1.041	1.0644

4	0.971	1.249	1.09	1.269	1.041	1.124
4.25	0.971	1.278	1.15	1.388	1.11	1.1794
4.5	0.951	1.278	1.179	1.398	1.14	1.1892
4.75	0.961	1.288	1.189	1.388	1.15	1.1952
5	0.951	1.219	1.239	1.497	1.17	1.2152
5.25	0.991	1.179	1.269	1.626	1.199	1.2528
5.5	1.09	1.16	1.378	1.695	1.219	1.3084
5.75	1.209	1.169	1.477	1.814	1.279	1.3896
6	1.467	1.219	1.546	1.873	1.298	1.4806
6.25	1.685	1.249	1.665	1.913	1.288	1.56
6.5	1.665	1.259	1.744	2.042	1.308	1.6036
6.75	1.596	1.288	1.824	2.081	1.308	1.6194
7	1.596	1.308	1.853	2.131	1.249	1.6274
7.25	1.615	1.368	1.744	2.151	1.229	1.6214
7.5	1.705	1.417	1.596	1.982	1.308	1.6016
7.75	1.853	1.556	1.417	1.576	1.516	1.5836
8	2.032	1.675	1.397	1.467	1.725	1.6592
8.25	2.22	1.903	1.368	1.437	1.943	1.7742
8.5	2.299	2.032	1.417	1.408	2.042	1.8396
8.75	2.379	2.022	1.477	1.229	2.062	1.8338
9	2.458	1.942	1.536	1.199	2.002	1.8274
9.25	2.498	1.933	1.615	1.189	1.962	1.8394
9.5	2.567	2.042	1.724	1.269	1.913	1.903
9.75	2.478	2.161	1.853	1.417	1.883	1.9584
10	2.359	2.289	1.982	1.586	1.824	2.008

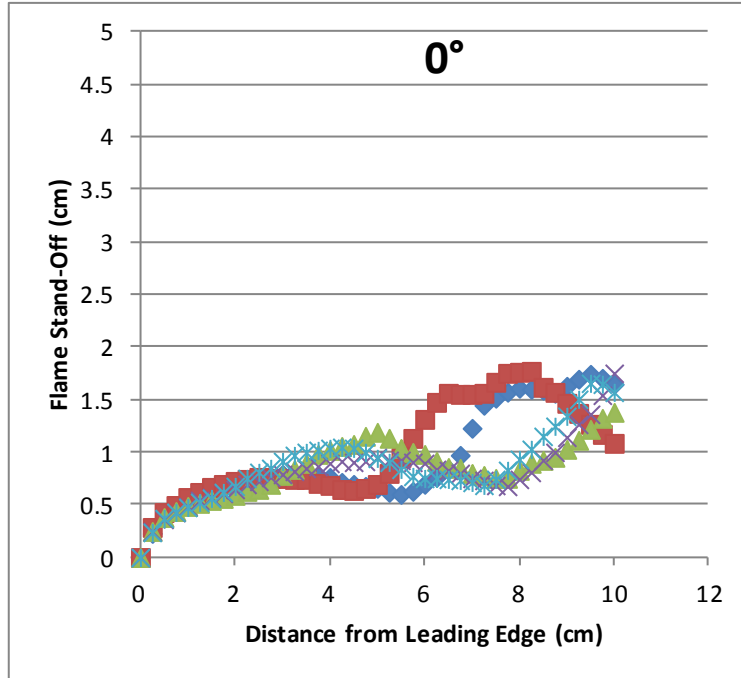


Figure 32: Data for methanol measured flame stand-off at 0°.

Table 12: Data for methanol measured flame stand-off at 0°.

0 Degrees						
x	y, Image 1	y, Image 2	y, Image 3	y, Image 4	y, Image 5	y, average
0	0	0	0	0	0	0
0.25	0.229	0.247	0.238	0.286	0.248	0.2496
0.5	0.372	0.362	0.371	0.428	0.381	0.3828
0.75	0.467	0.428	0.429	0.495	0.438	0.4514
1	0.524	0.485	0.476	0.571	0.486	0.5084
1.25	0.572	0.543	0.524	0.619	0.515	0.5546
1.5	0.619	0.571	0.562	0.667	0.543	0.5924
1.75	0.667	0.609	0.619	0.695	0.562	0.6304
2	0.715	0.647	0.676	0.724	0.591	0.6706
2.25	0.734	0.695	0.752	0.743	0.629	0.7106
2.5	0.762	0.724	0.81	0.762	0.648	0.7412
2.75	0.772	0.762	0.848	0.752	0.696	0.766
3	0.791	0.79	0.914	0.752	0.781	0.8056
3.25	0.8	0.819	0.971	0.743	0.838	0.8342
3.5	0.8	0.847	1	0.743	0.896	0.8572
3.75	0.781	0.866	1.019	0.705	0.981	0.8704

4	0.762	0.895	1.038	0.686	1.019	0.88
4.25	0.715	0.914	1.048	0.647	1.057	0.8762
4.5	0.696	0.905	1.038	0.638	1.076	0.8706
4.75	0.677	0.914	1	0.657	1.153	0.8802
5	0.658	0.952	0.943	0.695	1.191	0.8878
5.25	0.619	0.924	0.905	0.8	1.134	0.8764
5.5	0.6	0.924	0.838	0.952	1.038	0.8704
5.75	0.629	0.905	0.771	1.133	1	0.8876
6	0.696	0.895	0.752	1.314	0.981	0.9276
6.25	0.762	0.838	0.752	1.476	0.915	0.9486
6.5	0.838	0.828	0.743	1.562	0.857	0.9656
6.75	0.972	0.8	0.733	1.552	0.848	0.981
7	1.229	0.752	0.714	1.552	0.8	1.0094
7.25	1.448	0.733	0.686	1.562	0.781	1.042
7.5	1.515	0.685	0.743	1.667	0.753	1.0726
7.75	1.572	0.676	0.829	1.752	0.753	1.1164
8	1.61	0.743	0.933	1.762	0.829	1.1754
8.25	1.6	0.809	1.029	1.771	0.896	1.221
8.5	1.591	0.924	1.152	1.619	0.924	1.242
8.75	1.562	1	1.248	1.571	0.953	1.2668
9	1.629	1.143	1.343	1.467	1.029	1.3222
9.25	1.696	1.266	1.505	1.371	1.115	1.3906
9.5	1.743	1.362	1.657	1.267	1.219	1.4496
9.75	1.705	1.543	1.648	1.171	1.324	1.4782
10	1.648	1.752	1.571	1.086	1.381	1.4876

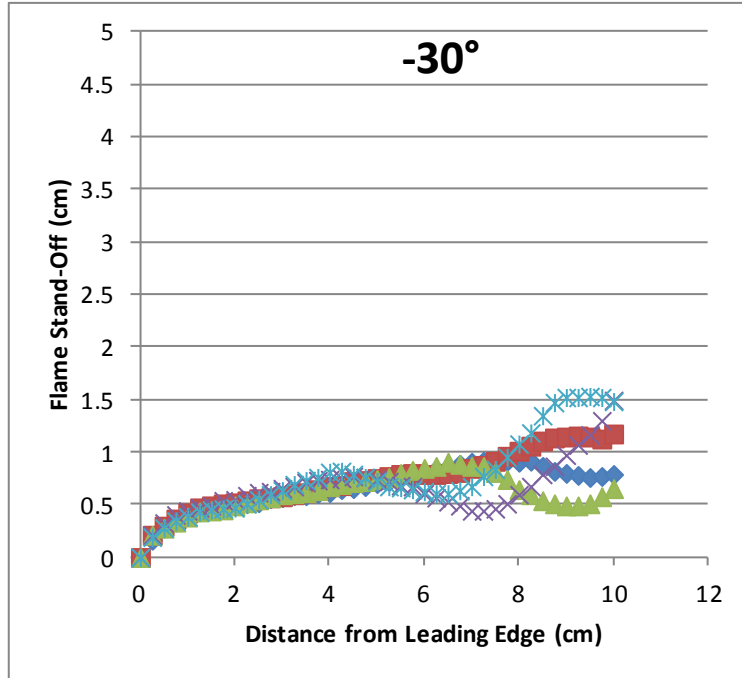


Figure 33: Data for methanol measured flame stand-off at -30° .

Table 13: Data for methanol measured flame stand-off at -30° .

-30 Degrees						
x	y, Image 1	y, Image 2	y, Image 3	y, Image 4	y, Image 5	y, average
0	0	0	0	0	0	0
0.25	0.164	0.212	0.193	0.212	0.212	0.1986
0.5	0.28	0.328	0.28	0.298	0.279	0.293
0.75	0.337	0.405	0.347	0.366	0.337	0.3584
1	0.395	0.443	0.386	0.424	0.385	0.4066
1.25	0.434	0.472	0.434	0.472	0.434	0.4492
1.5	0.453	0.492	0.453	0.491	0.443	0.4664
1.75	0.463	0.54	0.463	0.51	0.453	0.4858
2	0.501	0.549	0.472	0.52	0.491	0.5066
2.25	0.511	0.588	0.511	0.539	0.52	0.5338
2.5	0.521	0.617	0.549	0.559	0.549	0.559
2.75	0.559	0.627	0.598	0.568	0.569	0.5842
3	0.569	0.655	0.636	0.578	0.597	0.607
3.25	0.588	0.675	0.694	0.597	0.607	0.6322
3.5	0.588	0.713	0.732	0.616	0.617	0.6532
3.75	0.607	0.732	0.761	0.645	0.636	0.6762

4	0.617	0.742	0.81	0.674	0.674	0.7034
4.25	0.646	0.752	0.819	0.684	0.694	0.719
4.5	0.655	0.771	0.79	0.722	0.713	0.7302
4.75	0.675	0.761	0.761	0.732	0.723	0.7304
5	0.704	0.742	0.723	0.751	0.742	0.7324
5.25	0.723	0.723	0.675	0.77	0.761	0.7304
5.5	0.752	0.684	0.665	0.79	0.8	0.7382
5.75	0.771	0.675	0.646	0.799	0.829	0.744
6	0.819	0.607	0.627	0.79	0.848	0.7382
6.25	0.838	0.569	0.607	0.79	0.867	0.7342
6.5	0.858	0.53	0.607	0.799	0.906	0.74
6.75	0.887	0.492	0.636	0.809	0.886	0.742
7	0.906	0.443	0.675	0.848	0.867	0.7478
7.25	0.916	0.443	0.771	0.876	0.867	0.7746
7.5	0.916	0.463	0.838	0.915	0.809	0.7882
7.75	0.916	0.511	0.954	0.963	0.742	0.8172
8	0.906	0.598	1.079	1.011	0.646	0.848
8.25	0.916	0.675	1.185	1.059	0.597	0.8864
8.5	0.867	0.79	1.349	1.108	0.54	0.9308
8.75	0.819	0.867	1.474	1.137	0.511	0.9616
9	0.8	0.973	1.522	1.146	0.491	0.9864
9.25	0.781	1.07	1.522	1.156	0.491	1.004
9.5	0.761	1.166	1.532	1.146	0.511	1.0232
9.75	0.771	1.301	1.522	1.127	0.578	1.0598
10	0.79	1.494	1.484	1.175	0.655	1.1196

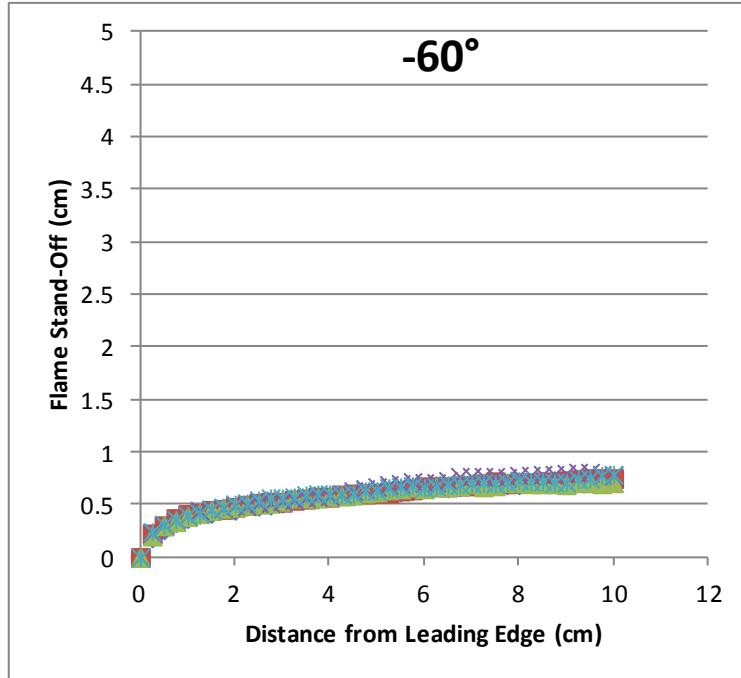


Figure 34: Data for methanol measured flame stand-off at -60° .

Table 14: Data for methanol measured flame stand-off at -60° .

-60 Degrees						
x	y, Image 1	y, Image 2	y, Image 3	y, Image 4	y, Image 5	y, average
0	0	0	0	0	0	0
0.25	0.186	0.224	0.204	0.233	0.244	0.2182
0.5	0.264	0.302	0.302	0.311	0.312	0.2982
0.75	0.332	0.37	0.341	0.36	0.361	0.3528
1	0.371	0.409	0.39	0.399	0.4	0.3938
1.25	0.41	0.419	0.419	0.447	0.419	0.4228
1.5	0.42	0.448	0.448	0.457	0.458	0.4462
1.75	0.459	0.458	0.468	0.467	0.478	0.466
2	0.449	0.477	0.477	0.496	0.507	0.4812
2.25	0.488	0.496	0.497	0.486	0.517	0.4968
2.5	0.488	0.516	0.507	0.516	0.546	0.5146
2.75	0.498	0.526	0.516	0.516	0.565	0.5242
3	0.517	0.526	0.536	0.535	0.565	0.5358
3.25	0.546	0.545	0.565	0.545	0.575	0.5552
3.5	0.556	0.555	0.565	0.564	0.595	0.567
3.75	0.556	0.574	0.565	0.574	0.604	0.5746

4	0.575	0.574	0.584	0.584	0.604	0.5842
4.25	0.585	0.594	0.584	0.603	0.595	0.5922
4.5	0.585	0.604	0.594	0.632	0.604	0.6038
4.75	0.614	0.604	0.614	0.652	0.634	0.6236
5	0.614	0.613	0.623	0.671	0.634	0.631
5.25	0.624	0.613	0.643	0.691	0.663	0.6468
5.5	0.624	0.633	0.653	0.701	0.672	0.6566
5.75	0.634	0.643	0.672	0.72	0.682	0.6702
6	0.673	0.672	0.653	0.71	0.663	0.6742
6.25	0.683	0.672	0.672	0.71	0.672	0.6818
6.5	0.663	0.672	0.672	0.73	0.692	0.6858
6.75	0.673	0.681	0.682	0.769	0.692	0.6994
7	0.692	0.681	0.701	0.769	0.702	0.709
7.25	0.692	0.701	0.672	0.769	0.711	0.709
7.5	0.683	0.72	0.682	0.769	0.702	0.7112
7.75	0.692	0.701	0.711	0.759	0.711	0.7148
8	0.692	0.711	0.711	0.779	0.731	0.7248
8.25	0.712	0.711	0.701	0.779	0.721	0.7248
8.5	0.722	0.72	0.701	0.788	0.721	0.7304
8.75	0.731	0.711	0.701	0.788	0.711	0.7284
9	0.712	0.73	0.692	0.798	0.711	0.7286
9.25	0.712	0.74	0.711	0.808	0.741	0.7424
9.5	0.712	0.75	0.711	0.808	0.75	0.7462
9.75	0.722	0.75	0.701	0.788	0.78	0.7482
10	0.712	0.75	0.711	0.779	0.789	0.7482

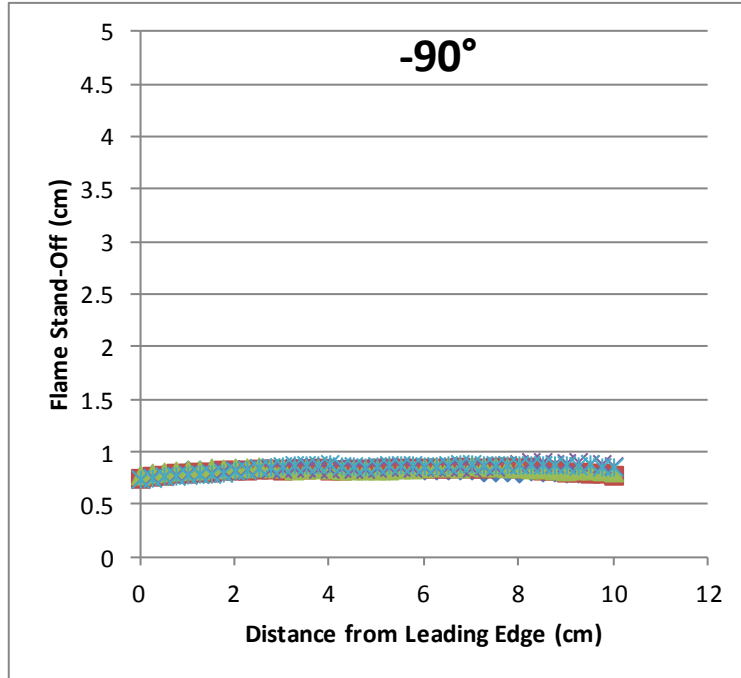


Figure 35: Data for methanol measured flame stand-off at -90° .

Table 15: Data for methanol measured flame stand-off at -90° .

x	-90 Degrees					y, average
	y, Image 1	y, Image 2	y, Image 3	y, Image 4	y, Image 5	
0	0.7745	0.7535	0.7845	0.7455	0.7455	0.7607
0.25	0.7935	0.7735	0.8035	0.7645	0.7545	0.7779
0.5	0.8035	0.7825	0.8135	0.7745	0.7745	0.7897
0.75	0.8035	0.8025	0.8235	0.7845	0.7745	0.7977
1	0.8325	0.8025	0.8325	0.7935	0.7845	0.8091
1.25	0.8325	0.8125	0.8325	0.7935	0.7935	0.8129
1.5	0.8325	0.8125	0.8525	0.8035	0.7935	0.8189
1.75	0.8235	0.8315	0.8425	0.8235	0.8035	0.8249
2	0.8325	0.8315	0.8525	0.8325	0.8235	0.8345
2.25	0.8425	0.8315	0.8525	0.8425	0.8325	0.8403
2.5	0.8425	0.8415	0.8615	0.8525	0.8525	0.8501
2.75	0.8525	0.8415	0.8525	0.8425	0.8615	0.8501
3	0.8525	0.8315	0.8525	0.8425	0.8715	0.8501
3.25	0.8615	0.8415	0.8325	0.8525	0.8815	0.8539
3.5	0.8615	0.8415	0.8425	0.8525	0.8815	0.8559
3.75	0.8615	0.8505	0.8425	0.8425	0.8815	0.8557

4	0.8615	0.8315	0.8425	0.8425	0.8915	0.8539
4.25	0.8525	0.8315	0.8325	0.8525	0.8715	0.8481
4.5	0.8425	0.8415	0.8325	0.8425	0.8715	0.8461
4.75	0.8325	0.8415	0.8325	0.8425	0.8615	0.8421
5	0.8325	0.8505	0.8325	0.8525	0.8715	0.8479
5.25	0.8325	0.8505	0.8325	0.8615	0.8815	0.8517
5.5	0.8425	0.8505	0.8425	0.8615	0.8815	0.8557
5.75	0.8425	0.8505	0.8425	0.8525	0.8815	0.8539
6	0.8325	0.8505	0.8525	0.8615	0.8715	0.8537
6.25	0.8325	0.8505	0.8615	0.8615	0.8715	0.8555
6.5	0.8325	0.8505	0.8615	0.8615	0.8815	0.8575
6.75	0.8325	0.8605	0.8525	0.8615	0.8915	0.8597
7	0.8325	0.8505	0.8715	0.8525	0.8915	0.8597
7.25	0.8135	0.8505	0.8615	0.8715	0.8815	0.8557
7.5	0.8135	0.8605	0.8615	0.8615	0.8815	0.8557
7.75	0.8135	0.8605	0.8525	0.8815	0.8815	0.8579
8	0.8035	0.8505	0.8525	0.8915	0.8815	0.8559
8.25	0.8235	0.8605	0.8425	0.9105	0.8815	0.8637
8.5	0.8135	0.8315	0.8425	0.9105	0.8815	0.8559
8.75	0.8135	0.8315	0.8325	0.8915	0.8815	0.8501
9	0.8035	0.8125	0.8235	0.9005	0.8815	0.8443
9.25	0.8035	0.8125	0.8325	0.9105	0.8715	0.8461
9.5	0.8035	0.8025	0.8325	0.8915	0.8915	0.8443
9.75	0.8135	0.8025	0.8235	0.8915	0.8615	0.8385
10	0.8035	0.7825	0.8135	0.8715	0.8615	0.8265

Heat Flux:

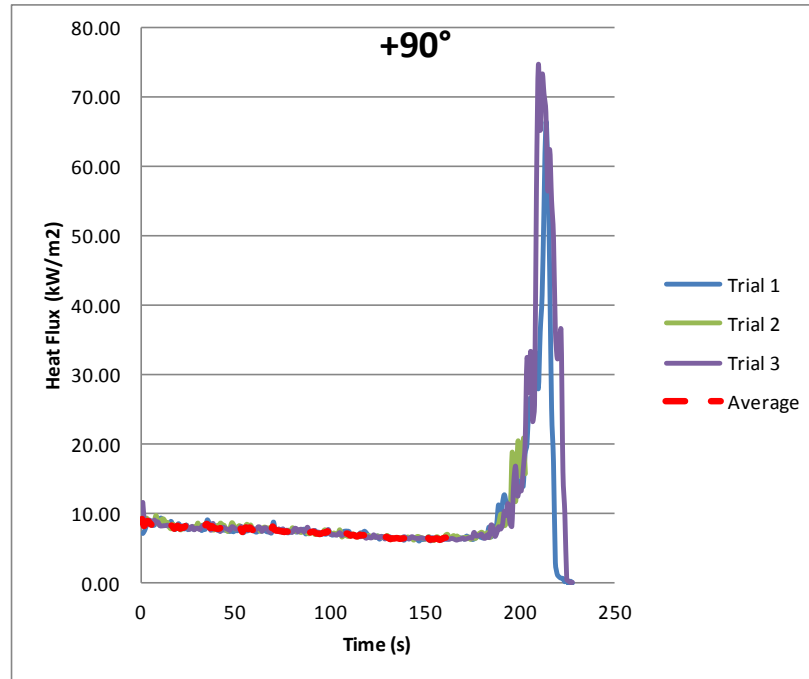


Figure 36: Individual and average heat flux test readings for methanol on 10 x 10 wick at +90°.

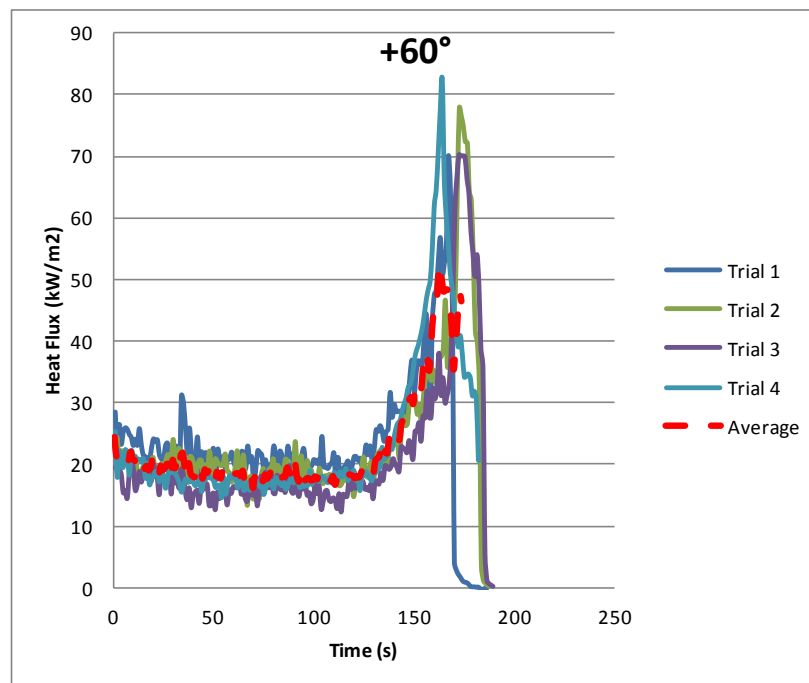


Figure 37: Individual and average heat flux test readings for methanol on 10 x 10 wick at +60°.

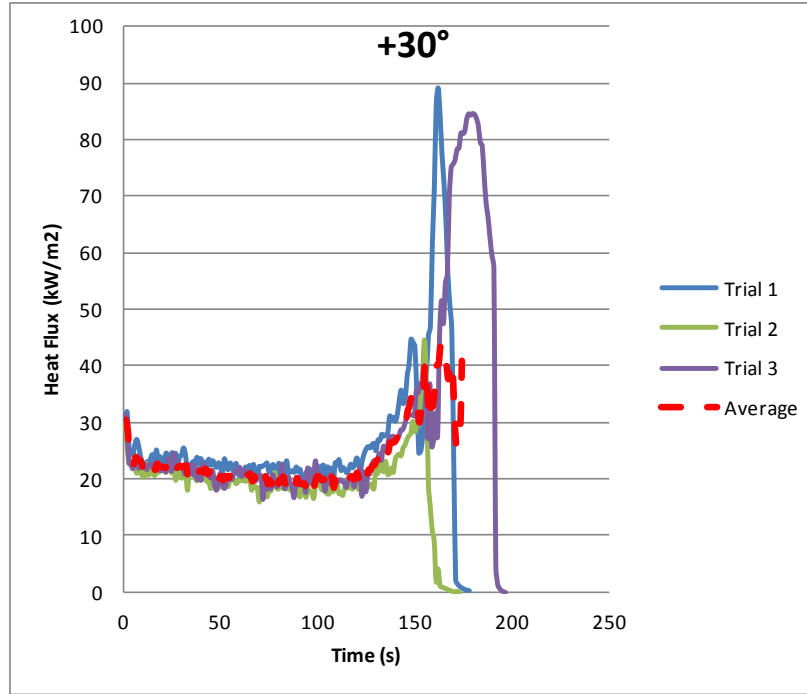


Figure 38: Individual and average heat flux test readings for methanol on 10 x 10 wick at +30°.

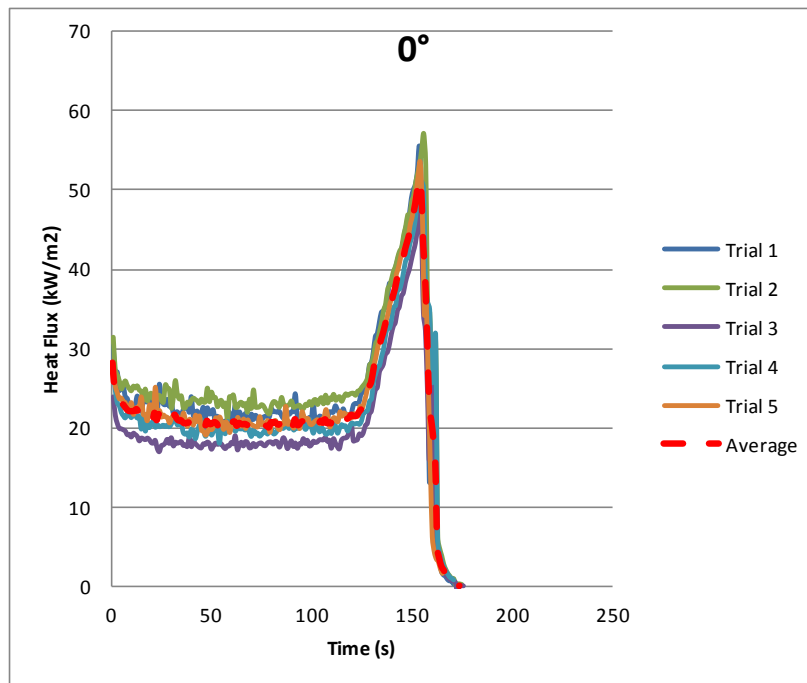


Figure 39: Individual and average heat flux test readings for methanol on 10 x 10 wick at 0°.

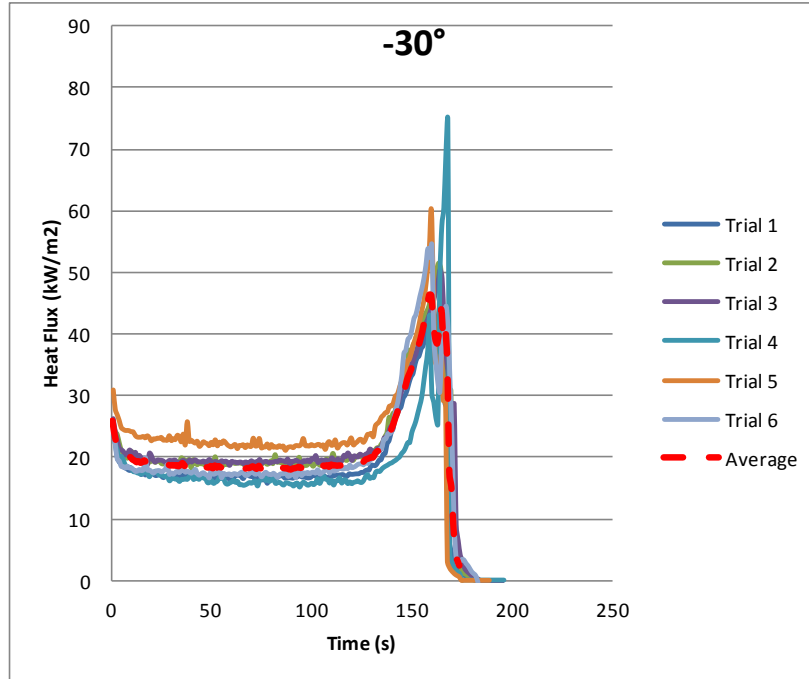


Figure 40: Individual and average heat flux test readings for methanol on 10 x 10 wick at -30°.

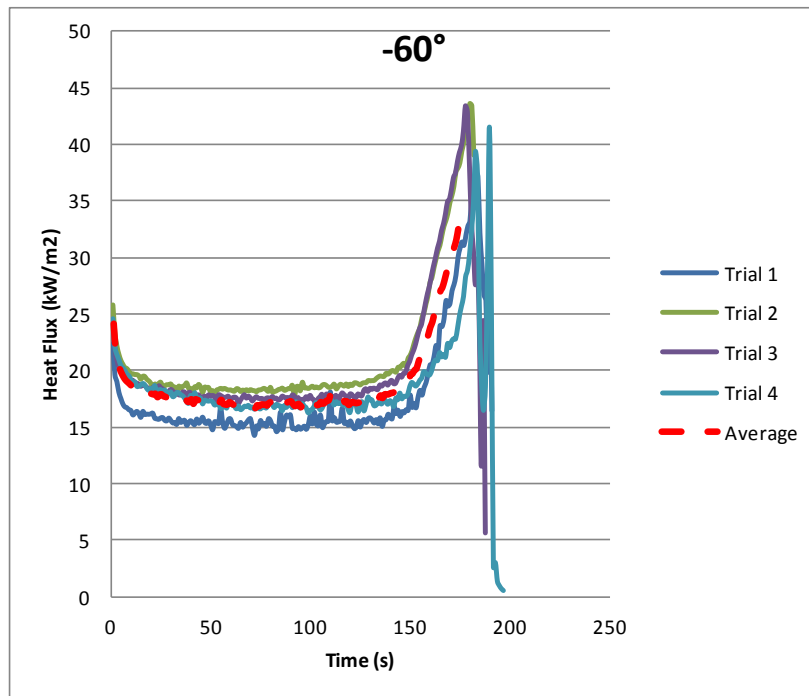


Figure 41: Individual and average heat flux test readings for methanol on 10 x 10 wick at -60°.

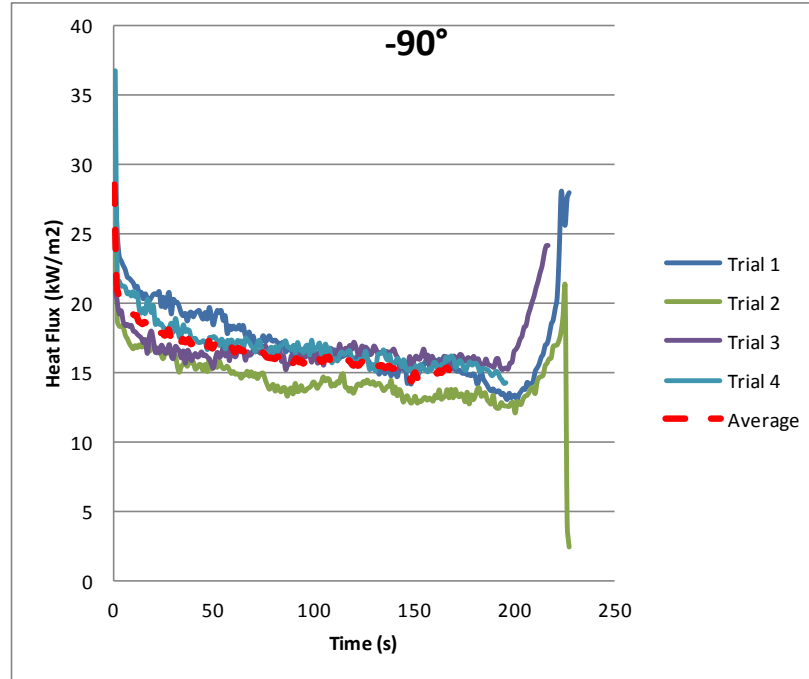


Figure 42: Individual and average heat flux test readings for methanol on 10 x 10 wick at -90° .

Appendix B: 1g Ethanol Experimental Data

Table 16: 1g Ethanol Experimental Data

Fuel	Orientation	Pyrolysis Length (cm)	Burning Rate (g/m ² -s)
Ethanol	90	1	28.47
	90	2	21.65
	90	3	18.87
	90	4	16.19
	90	6	14.89
	90	8	14.36
	90	10	13.95
	60	1	30.82
	60	2	23.32
	60	3	20.49
	60	4	18.38
	60	6	16.32
	60	8	15.87
	60	10	14.98
	30	1	32.50
	30	2	24.85
	30	3	22.06
	30	4	19.02
	30	6	16.97
	30	8	15.71
	30	10	15.11
	0	1	30.58
	0	2	24.12
	0	3	21.27
	0	4	18.29
	0	6	16.65
	0	8	15.74
	0	10	14.57
	-30	1	26.24
	-30	2	21.92
-30	3	19.63	
-30	4	17.52	
-30	6	16.22	
-30	8	14.95	
-30	10	14.43	
-60	1	23.55	
-60	2	18.94	
-60	3	17.21	

-60	4	15.76
-60	6	13.88
-60	8	13.53
-60	10	13.15
-90	1	18.34
-90	2	15.23
-90	3	13.97
-90	4	12.76
-90	6	12.34
-90	8	11.36
-90	10	11.06

Appendix C: 0g Ethanol Experimental Observations
Airplane Video Snapshots: Approximately every 3 seconds after ignition



Figure 43: Snapshots from "Zero 2" Video

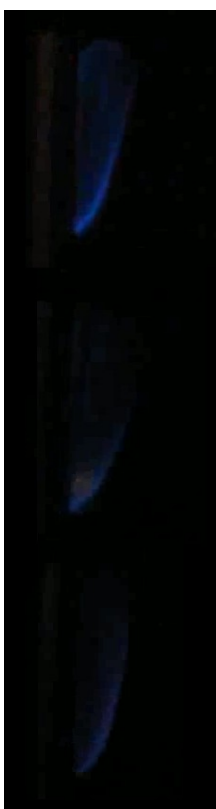


Figure 44: Snapshots from "Zero 3" Video

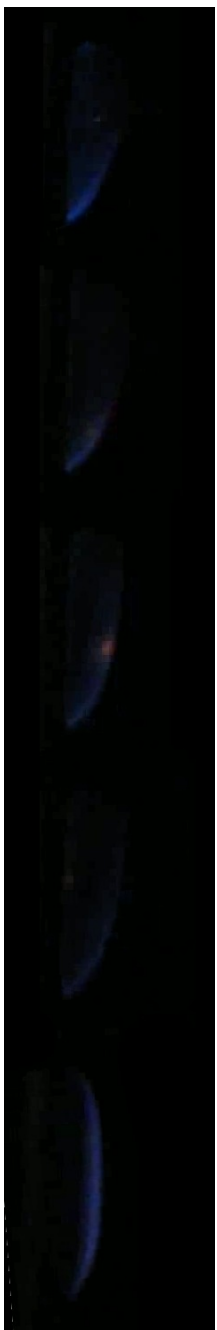


Figure 45: Snapshots from "Zero 4" Video

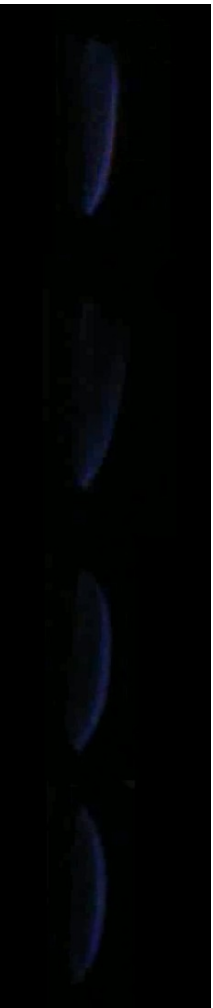


Figure 46: Snapshots from “Zero 5” Video

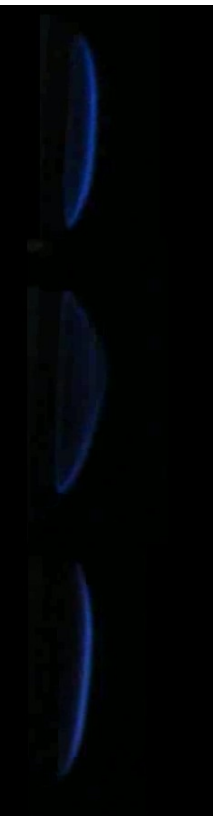


Figure 47: Snapshots from “Zero 6” Video

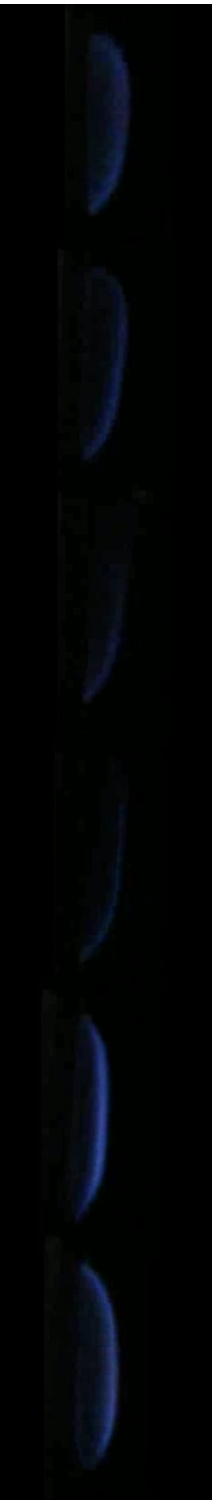


Figure 48: Snapshots from “Zero 8” Video



Figure 49: Snapshots from “Zero 11” Video



Figure 50: Snapshots from “Zero 12” Video

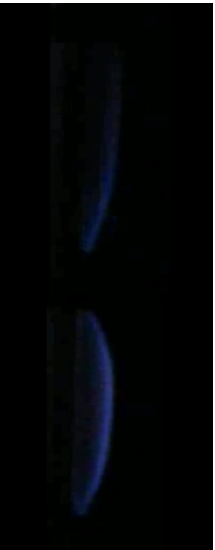


Figure 51: Snapshots from “Zero 13” Video

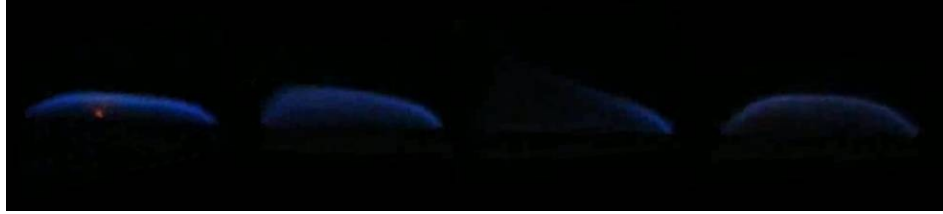


Figure 52: Snapshots from “Zero 14” Video

Due to the nature of the filming as a consequence of using a hand-held personal video camera not all tests provided a good consistent view of the flame. Snapshots from these videos have been excluded. Specifically, videos 1, 7, and 9 all had issues. Two of these were attempts at capturing the flame through an alternate view port (rather unsuccessfully) and some of the videos had issues with maintaining a view of the flame due to the operators floating out of position. Snapshots from test 10 (spiraling base observed) were excluded as there is already a sequence in the text of this thesis.

Drop Tower Video Snapshots: Approximately every second after release of the vehicle



Figure 53: Snapshots from first drop, using Ethanol on a 1 x 4 cm wick. Ignition took place approximately 3 seconds before release. Flame showed unsteady behavior but lasted the duration of the drop.



Figure 54: Snapshots from second drop, using Ethanol on a 1 x 4 cm wick. Ignition approximately a half second after release of the vehicle. Flame self-extinguished after about a second, the above photographs are not every second, instead they were chosen more frequently to show in which way the flame extinguished.



Figure 55: Snapshots from third drop utilizing Ethanol on a circular pyrolysis area with equivalent area to the 1 x 4 cm rectangular wicks used in the previous two drops. Ignition approximately a half second before release. Although difficult to see, flame was sustained for duration of the drop.



Figure 56: Snapshots from fourth drop utilizing Ethanol on a 5 cm diameter circular wick. Ignition took place approximately a half second before release. Flame Self extinguished between 1 and 2 seconds after release.



Figure 57: Snapshots from fifth drop, Ethanol on a 5 cm diameter circular wick in 30% oxygen atmosphere. Ignition approximately a half second before release. Flame sustained for entire duration of the drop. Flame front expanded slowly over the course of the drop.

Appendix D: Observed transition to unsteadiness

Flames displayed a transition to unsteadiness as marked approximately in Figure 15. This transition was observed in the form of a flapping behavior and typically this onset position varied in and out with x over the course of the test. Figure 58 shows the range at which the onset of unsteadiness was observed in terms of Grashof number as a function of orientation. Ranges displayed convey maximum and minimum values.

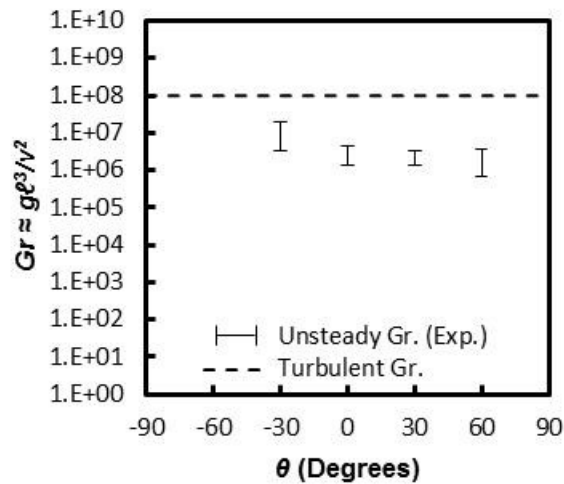


Figure 58: Transition to unsteadiness as a function of orientation. Range shows maximum and minimum observed in the five analyzed flame stand-off photographs.

References

- [1] T. Ahmad, and G.M. Faeth, “An Investigation of the Laminar Overfire Region Along Upright Surfaces”, *Journal of Heat Transfer*, Vol. 100, 1978, pp. 112-119.
- [2] T. Ahmad, “Investigation of the Combusting Region of Fire-Induced Plumes Along Upright Surfaces”, Ph.D. Thesis, The Pennsylvania State University, 1978.
- [3] T. Ahmad, and G.M. Faeth, “Turbulent Wall Fires”, *Seventeenth Symposium (Intl.) on Combustion*, The Combustion Institute, Pittsburgh, PA, 1979, pp. 1149-1160.
- [4] S. Ali, V. Raghavan, and A. Rangwala, “A Numerical Study of Quasi-steady Burning Characteristics of a Condensed Fuel: Effect of Angular Orientation of Fuel Surface”, *Combustion Theory and Modeling*, Vol. 14, No. 4, 2010, pp. 495-518.
- [5] P.L. Blackshear Jr., and K.A. Murty, “Heat and Mass Transfer to, from, and within Cellulosic Solids Burning in Air”, *Tenth Symposium (Intl.) on Combustion*, The Combustion Institute, Pittsburgh, PA, 1965, pp. 911-923.
- [6] P.L. Blackshear Jr., and K.A. Murty, “Some Effects of Size, Orientation, and Fuel Molecular Weight on the Burning of Fuel-Soaked Wicks”, *Eleventh Symposium (Intl.) on Combustion*, The Combustion Institute, Pittsburgh, PA, 1967, pp. 545-552.
- [7] M.J. Bustamante, K.T. Dotson, Y. Zhang, P.B. Sunderland, J.G. Quintiere, “Laminar Burning of Flat Diffusion Flames at Various Orientations”, Central States Section of the Combustion Institute, Dayton (Apr. 2012) 15 pp.

- [8] J. DeRis, and L. Orloff, "The Role of Buoyancy Direction and Radiation in Turbulent Diffusion Flames on Surfaces", *Fifteenth Symposium (Intl.) on Combustion*, The Combustion Institute, Pittsburgh, PA, 1975, pp. 175-182.
- [8] S. Elonen-Wright (NASA Official), S. Maier (Ed.), National Aeronautics and Space Administration (NASA) Zero Gravity Research Facility. [Online]. Available from: <http://facilities.grc.nasa.gov/zerog/>. Accessed July 2012.
- [10] E.G. Groff and G.M. Faeth, "Laminar Combustion of Vertical Free-Standing Fuel Surfaces", *Combustion and Flame*, Vol. 32, 1978, pp. 139-150.
- [11] J.S. Kim, J. DeRis, and F.W. Kroesser, "Laminar Free-Convective Burning of Fuel Surfaces", *Thirteenth Symposium (Intl.) on Combustion*, The Combustion Institute, Pittsburgh, PA, 1971, pp. 949-961.
- [12] F.J. Kosdon, F.A. Williams, and C. Buman, "Combustion of Vertical Cellulosic Cylinders in Air", *Twelfth Symposium (Intl.) on Combustion*, The Combustion Institute, Pittsburgh, PA, 1967, pp.545-552.
- [13] G.A. Marxman, *Sixteenth Symposium (Intl.) on Combustion*, The Combustion institute, Pittsburgh, PA, 1977, pp. 1345-1354.
- [14] L. Orloff, and J. DeRis, "Cellular and Turbulent Ceiling Fires", *Combustion and Flame*, Vol. 18, 1972, pp. 389-401.
- [15] L. Orloff, and J. DeRis, "Modeling of Ceiling Fires", *Thirteenth Symposium (Intl.) on Combustion*, The Combustion Institute, Pittsburgh, PA, 1971, pp. 979-992.
- [16] J. Quintiere, *Fundamentals of Fire Phenomena*, 1st Edition, John Wiley and Sons Ltd., West Sussex, England, 2006.

- [17] H.D. Ross (Ed.), *Microgravity Combustion: Fire in Freefall*, Combustion Treatise, Academic Press, San Diego, CA, USA (2001) p. 4.
- [18] T. St. Onge (NASA Official), National Aeronautics and Space Administration (NASA) Ground-Based Facilities. [Online]. Available from: http://microgravity.grc.nasa.gov/ground/flight_aircraft.htm. Accessed July 2012.
- [19] P. M. Struk, D. L. Dietrich, and J. S. Tien, "Large droplet combustion experiment using porous spheres conducted in reduced gravity aboard an aircraft - Extinction and the effects of g-jitter," *Microgravity Science and Technology* Vol. 9, No. 2, 1996. pp. 106-116.
- [20] Y.-X. Tao and M. Kaviany, "Burning Rate of Liquid Supplied Through a Wick", *Combustion and Flame*, Vol. 86, 1991, pp. 47-61.